National Aeronautics and Space Administration

# Modeling gas-dust plumes and an application to comet outbursts

**Author: A. Gicquel (3222)**
**P. von Allmen (3980), M. Hofstadter (3222), A. Lethuillier (3222)**

## Introduction

Gas-dust interactions are fundamental processes found on many solar system objects. The Cassini spacecraft discovered plumes, emanating from Saturn's moon, Enceladus. The Hubble Telescope has observed plumes erupting from Jupiter's moon, Europa. Geyser-like eruptions were discovered in Voyager 2 images of Triton, Neptune's satellite. Recent missions have returned extraordinary data from icy bodies in the solar system, including the Rosetta Mission, which successfully observed outbursts from the nucleus of comet 67P/Churyumov-Gerasimenko (67P)

Triton: Credit: NASA Voyager 2 Mission

## Methodology

To understand the nature of jets from the nucleus of Comet 67P, and to study the formation of the coma and surface activity, we will analyze and interpret data from two cameras, OSIRIS (Optical, Spectroscopic, and Infrared Remote Imaging System) and NAVCAM, and from the MIRO (Microwave Instrument for the Rosetta Orbiter) instrument. The OSIRIS and NAVCAM cameras are more sensitive to the detection of dust, and the MIRO instrument is more sensitive to the detection of gas.

### Coma gas model

**Assumed**
- Optically thin
- Collisionless model
- Temperature at the surface of the nucleus and the gas production driven by the solar illumination.

**Derived**
- Gas outgassing rate ( $Q_{gas}$ ), used a boundary condition for the calculation of the gas density, velocity and temperature profiles

### Dust model

**Assumed**
- Forces acting on the grains: Drag force , gravity and radiative pressure

**Derived**
- Dust production rate ($Q_{dust}$)
- Theoretical Brightness

The theoretical brightness (W m$^{-2}$ nm$^{-1}$ sr$^{-1}$) produced by a collection of grains of various radii will be compared with OSIRIS/ NAVCAM :

$$\text{Brightness} = \frac{Q_{dust} V_n}{v(a)} \frac{F_{Sun}}{R_h^2} \frac{1}{4\pi} \frac{1}{A_{px}} \int_{a_{min}}^{a_{max}} \frac{\pi a^2}{\Delta_{S/C}^2} Q_{scat}(a,\lambda) p(a,\lambda,\Theta) n(a) da$$

Where $Q_{dust} \propto Q_{gas}$ is the dust outgassing rate ($Q_{gas}$ [kg m$^{-2}$ s$^{-1}$] is from the gas coma model), $v(a)$is the dust velocity and $V_n$ is the volume of the element, $F_{Sun}$ = 1.5650 W m$^{-2}$ nm$^{-1}$ is the solar flux, $R_h$= 1.25 AU is the heliocentric distance, $A_{px}$ = 3.5x10$^{-10}$ sr is the solid angle of a single pixel, $\Delta_{S/C}$ =186 km is the distance between the spacecraft and the comet, $a$ is the radius of the particle, $\lambda$ = 642 nm is the wavelength, $Q_{scat}$ is the scattering coefficient, $p$ is the phase function, $\Theta$ is the phase angle, and $n(a)da$ is the size distribution. $Q_{scat}$ and $p$ are obtained from the Mie theory and are dependent of the dust composition (we model pure carbon, pure silicates or a 50/50 mixture) and the size of the grains ($0.5\mu$m – 95 $\mu$m).

67P: Credit: ESA/OSIRIS

## Result

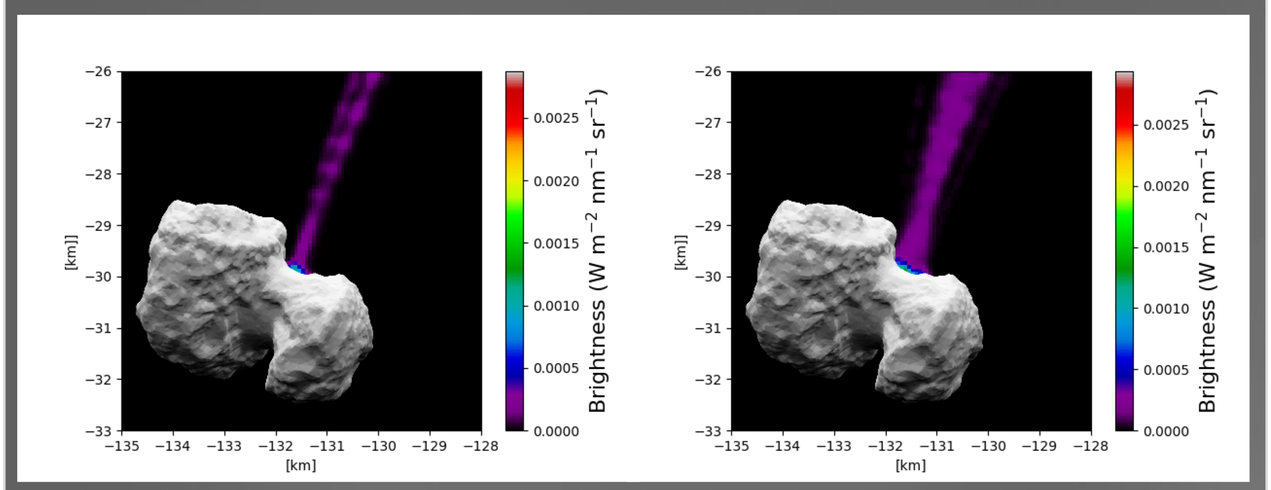


a. active region 200m around the source location $Q_{dust}/Q_{gas}$= 3.5

b. active region 400m around the source location $Q_{dust}/Q_{gas}$= 2

Fig 1. Brightness of the outburst for a dust composition 50% Carbon 50% Silicate

Simulations with pure carbon and silicates give a similar shape/opening angle however we need $Q_{dust}/\ Q_{gas}$= 7 for pure carbon and $Q_{dust}/\ Q_{gas}$= 0.5 for pure silicates grains with an active region =200m.

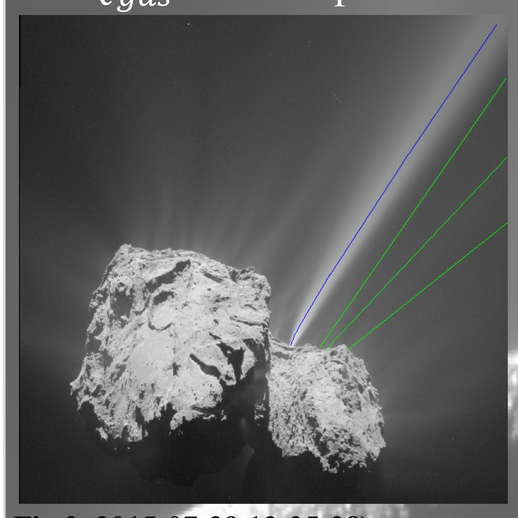

**Fig 2. 2015-07-29 13:25:28) (OSIRIS NAC FOV: 7 x 7 km, Gicquel et al. (2017)**

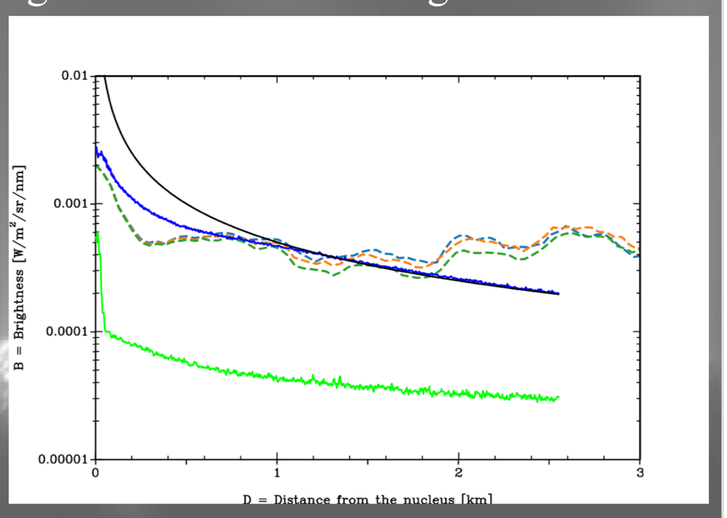


Fig 3. Blue: Radial profile for the outburst. Green: Radial profile for the coma background from OSIRIS Black: Radial profile over a cone. Gicquel et al. (2017). Dashed-line: Radial profile for the outburst from the simulations

Using this method we reproduced the overall shape of the radial profile for the outburst. We will add the radius of curvature in our simulation to correct the increase of the brightness after 2km.

Enceladus: Credit: NASA/JPL-Caltech/SSI

## Conclusion and Future Work

- We have not yet done retrievals, but find that reasonable assumptions used to model nucleus and coma processes yield simulated jets that have the correct basic morphology observed by the cameras, and have gas/dust ratios consistent with various Rosetta spacecraft measurements. In particular:
  - -The size of the active region controls the jet opening angle in our model.
  - - 0.8< $Q_{dust}/Q_{gas}$<10 in agreement with various estimates (Rotundi et al. 2015, Gicquel et al. 2017).
- We are working to improve the resolution of the model (both in spatial coordinates and in dust-grain size bins) in order to create smoother looking simulated jets for quantitative comparison to images.
- We also intend to account for optically thick dust jets, and model gas spectral emissions for comparison to MIRO submilliimeter observations.
- We will then run simulations for several of the outbursts observed in the summer of 2015 (Vincent et al. 2016).

While Enceladus, Triton and Europa have clear differences from comets, they are icy bodies as well, with similar processes seen in the multiple outbursts observed with the Rosetta instruments.

Europa: Credit: NASA/ESA/W. Spark (STScI)/USGS Astrogeology Science Center

**National Aeronautics and Space Administration**
**Jet Propulsion Laboratory**
California Institute of Technology
Pasadena, California

www.nasa.gov



Gicquel, A., Rose, M., Vincent, J-B. et al. 2017, MNRAS, 469, S178
Rotundi, A., Sierks, H., Della Corte, V. et al. 2015, Science, 347
Vincent. J-B, A'Hearn. M., Lin. Z-Y. et al. 2016, MNRAS, 462, S184

**Poster No. P-01**

**National Aeronautics and Space Administration**
**Jet Propulsion Laboratory**
California Institute of Technology
Pasadena, California

www.nasa.gov



National Aeronautics and Space Administration

# Minor species in Jupiter's troposphere from ground-based spectroscopy

**Rohini Giles[1]**

**Glenn Orton[1], James Sinclair[1], Leigh Fletcher[2], Patrick Irwin[3]**

**[1]Section 322, JPL/Caltech, [2]University of Leicester, [3]University of Oxford**

## 1. Introduction

- Minor species in Jupiter's atmosphere play an important role in understanding the planet's complex meteorology
- Disequilibrium species: **$GeH_4$, $AsH_3$ and $PH_3$**
  - Can only be observed in troposphere because of rapid vertical motion forcing them upwards from the deeper parts of the planet where they exist in equilibrium [1]
- Condensable species: **$NH_3$**
  - Forms clouds of both $NH_3$ ice and solid $NH_4SH$ in the troposphere [2], giving the gas a complex vertical distribution
- Because volume mixing ratios vary with altitude, these species act as tracers for atmospheric dynamics → observations of their spatial distributions can be used to constrain global circulation patterns in the troposphere [1]

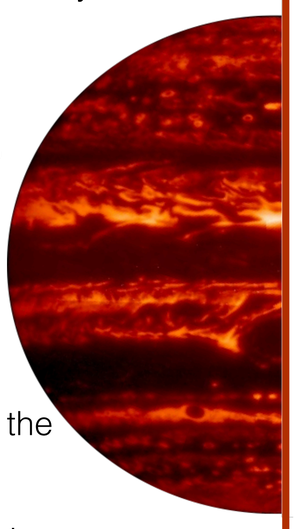

*Jupiter at 4.8 μm, observed by Gemini/NIRI. The tropospheric clouds are backlit by the bright radiation from deep in the atmosphere. Credit: Gemini Observatory / AURA /NSF / UC Berkeley*

- Gases can be studied using 5-μm spectral region → atmospheric window, probes pressures of 2-6 bar
- VLT/CRIRES [3] used to take high spectral resolution (R=96,000) observations of $GeH_4$, $AsH_3$, $PH_3$ and $NH_3$ lines at 5-μm. Slit aligned north-south along central meridian → see how line shape (and hence abundance) varies with latitude

## 2. Retrieval method

- CRIRES spectra were fitted using the NEMESIS radiative transfer and retrieval algorithm [4]
  - Multiple-scattering radiative transfer forward model calculates observed top-of-atmosphere spectral radiance for a given set of atmospheric parameters
  - Atmospheric parameters are iteratively adjusted to match the observed spectrum, following an optimal estimation approach
  - Initially assumed single cloud layer at 0.8-bar, variable opacity, scattering properties from [5]
  - $GeH_4$, $AsH_3$, $PH_3$ → allowed to vary via single scaling factor, assumed to be well-mixed
  - $NH_3$ → abundance allowed to vary continuously (more lines observed so more vertical information obtained)

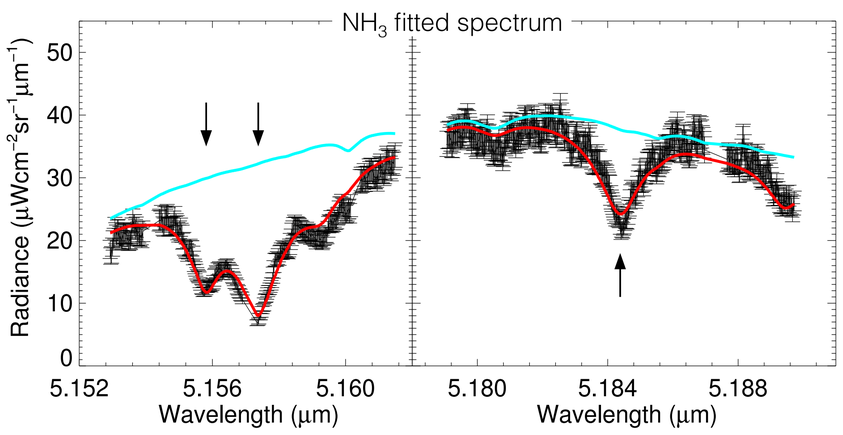


*Example of a CRIRES spectrum (black) with $NH_3$ absorption features marked by arrows. Spectrum is from the warm South Equatorial Belt. The NEMESIS best-fit spectrum is shown in red, along with a synthetic spectrum showing what it would look like in the absence of $NH_3$ (blue).*

## 3. Latitudinal retrieval results

### a) $GeH_4$ [6]

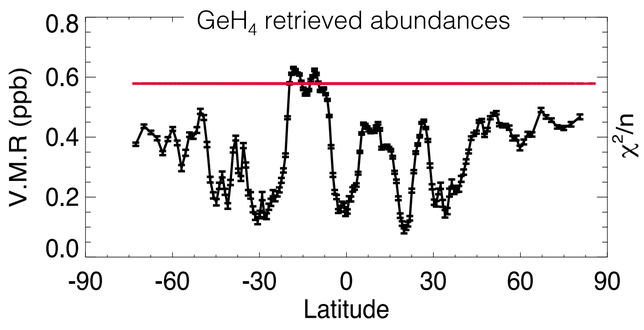


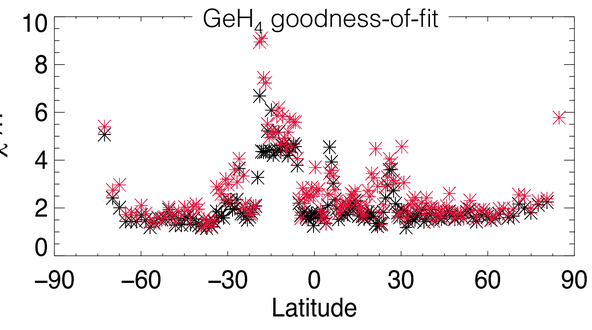


*Black: retrieved $GeH_4$ abundance and goodness-of-fit as a function of latitude. Red: the goodness-of-fit that can be obtained when $GeH_4$ is held constant and opacity of a 5-bar cloud is allowed to vary instead.*

- Initial retrieval (black) shows apparent belt-zone variability in $GeH_4$ abundance
- However, holding $GeH_4$ constant and allowing the opacity of a deep (5-bar) cloud to vary instead (opaque in zones, transparent in belts [6][7]) produces comparable quality fits → no evidence for latitudinal variability in $GeH_4$ [7]

### b) $AsH_3$ and $PH_3$ [6]

*As above but for $AsH_3$ → abundance and goodness-of-fit with freely varying $AsH_3$ (black) vs fixed $AsH_3$ (red)*

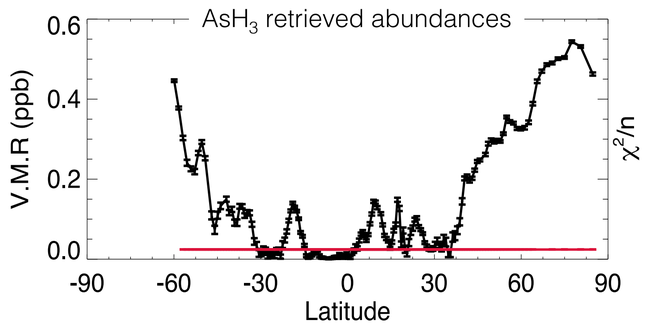


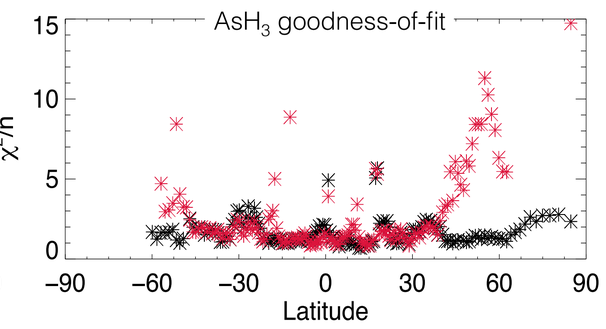


*As above but for $PH_3$ → abundance and goodness-of-fit with freely varying $PH_3$ (black) vs fixed $PH_3$ (red)*

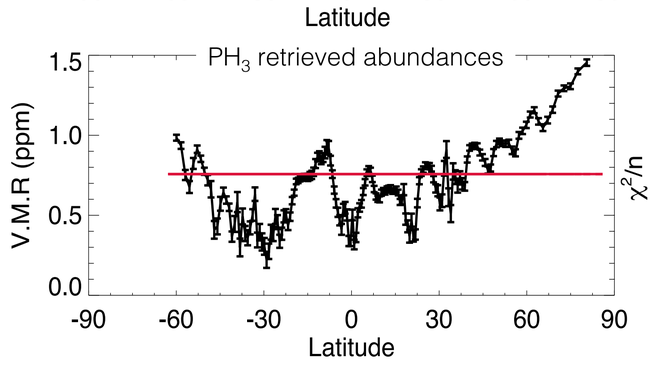


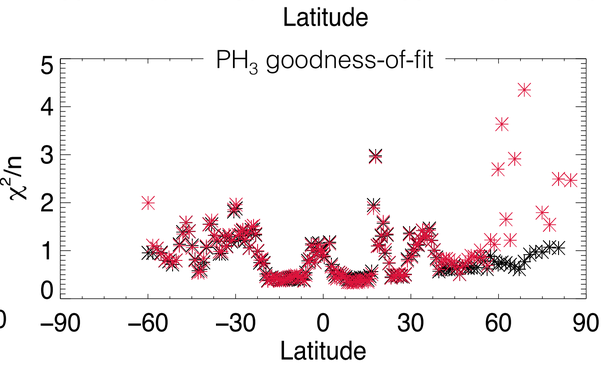


- $AsH_3$ and $PH_3$ both show enhancement in abundance towards poles
- Attempting to hold abundance constant and allow deep clouds to vary instead causes significant worsening of the fits → evidence for latitudinal variability in $AsH_3$ and $PH_3$ [7]

### c) $NH_3$ [8]

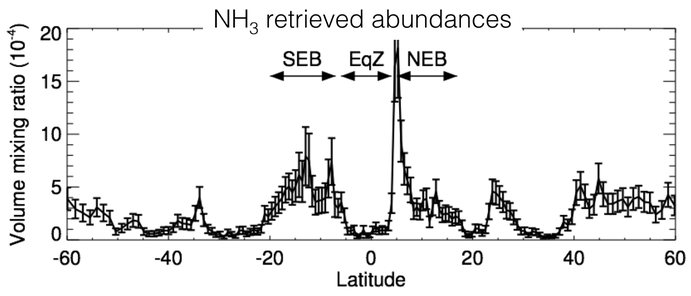


*Retrieved $NH_3$ abundance at 3.3 bar – $NH_3$ volume mixing ratio is allowed to vary continuously, single cloud layer used for this retrieval*

- $NH_3$ retrievals show apparent belt-zone variability, but as with $GeH_4$ this can equally be explained by deep cloud variability
- However, large spike in abundance on boundary of Equatorial Zone and North Equatorial Belt is genuine

## 4. Conclusions

- Apparent belt-zone variability in molecular abundances can sometimes be explained by the deep cloud structure – be cautious!
- Disequilibrium species: $GeH_4$, $AsH_3$, $PH_3$
  - CRIRES observations → $AsH_3$ and $PH_3$ have enhancement at high latitudes, $GeH_4$ has no evidence for latitudinal variability
  - Theoretical study [9] → $GeH_4$ should have enhancement at low latitudes, $AsH_3$ and $PH_3$ should have no latitudinal variability
  - Possible explanations: planetary-scale motion at the poles? photolytic effects? missing/poorly constrained chemical reactions?
- Condensable species: $NH_3$
  - Deep cloud complicates comparison of belts + zones, but even with opaque equatorial cloud, it is difficult to reproduce high abundance seen by Juno/MWR [10]
  - Spike in abundance on EqZ/NEB boundary consistent with both MWR [10] and ammonia 'plumes' previously seen at higher altitudes (~500 mbar) [11]

[1] Taylor et al. (2004). Jupiter: The Planet, Satellites and Magnetosphere, CUP
[2] Atreya et al. (1999). Planet. Space Sci., 47(10), 1243-1262
[3] Käufl et al. (2004). Proc. SPIE, 5492
[4] Irwin et al. (2008). J. Quant. Spectrosc. Radiat. Transfer, 109(6), 1136-1150
[5] Giles et al. (2015). Icarus, 257, 457-470
[6] Giles et al. (2017a). Icarus, 289, 254-269
[7] Bjoraker et al. (2015). Astrophys. J., 810(2), 122
[8] Giles et al. (2017b). GRL, 44(21), 10838-10844
[9] Wang et al. (2016). Icarus, 276, 21-38
[10] Li et al. (2017). GRL, 44(11), 5317-5325
[11] Fletcher et al. (2016). Icarus (278), 128-161

**Poster No. P-02**

National Aeronautics and Space Administration

# Looking for seasonal changes on comet Churyumov-Gerasimenko with MIRO

**Author: Anthony Lethuillier (3222)**
**Paul A, Von Allmen (3980) and Mark D, Hofstadter (3222)**

## Context and area observed

- One of objectives of the European Space Agency Rosetta mission was to study and better understand the 67P/Churyumov–Gerasimenko comet and the processes affecting it.
- As part of this effort the Microwave Instrument for the Rosetta Orbiter (MIRO) performed broadband, continuum measurements at 188 GHz and 562 GHz of the nucleus and coma from August 2014 to September 2016.
- The Imhotep region, located on the main lobe of the nucleus, presents a smooth terrain surrounded by rougher rocky terrain. For this study we focused exclusively on the smoother regions, which are easier to model.
- This area was observed twice by MIRO, the first time on October 27 2014 as a single swath observation then again on July 9 2016 as a raster scan (see Figure 1).
- The smooth regions of Imhotep are known to be a gravitational low (Auger et al. 2014), and may be smooth because dust collects there. We calculate gravitational potential using a 3D nucleus shape model, and use this to identify the regions of interest (areas in green and blue in Figure 2).

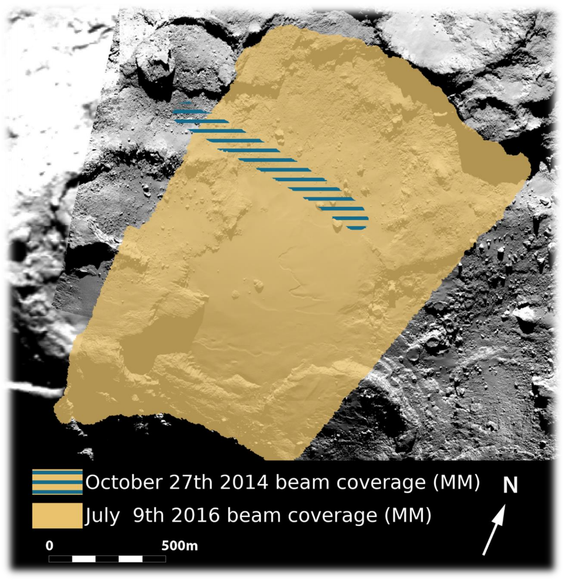


*Figure 1: Areas observed by MIRO during the October 2014 and July 2016 scans*

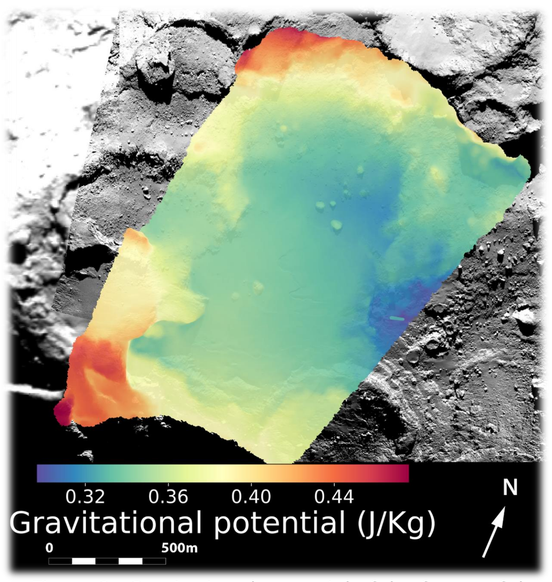


*Figure 2: Gravitational potential of the facets of the shape model. The measurements over of the blue and green areas were then used for this study*

## Model & method

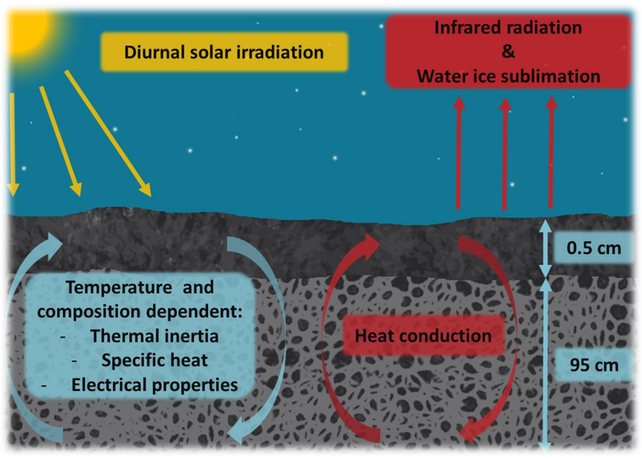


*Figure 3: Schematic representation of the 1D thermal model used in this study*

- Using the 3D shape model of the nucleus we are able, for each MIRO measurement during the scan, to determine the diurnal solar illumination of the surface area observed.
- Combining this information with a 1D thermal model (see Figure 3) and a radiative transfer model we are able to constrain the physical properties of the subsurface of the nucleus by finding the best fitting modelled brightness temperatures to the measured ones.
- The sounding depth is 1 cm at sub-mm wavelengths and 10 cm at mm wavelength. This gives us the possibility to use a two layer model of the subsurface.




## Results and interpretation

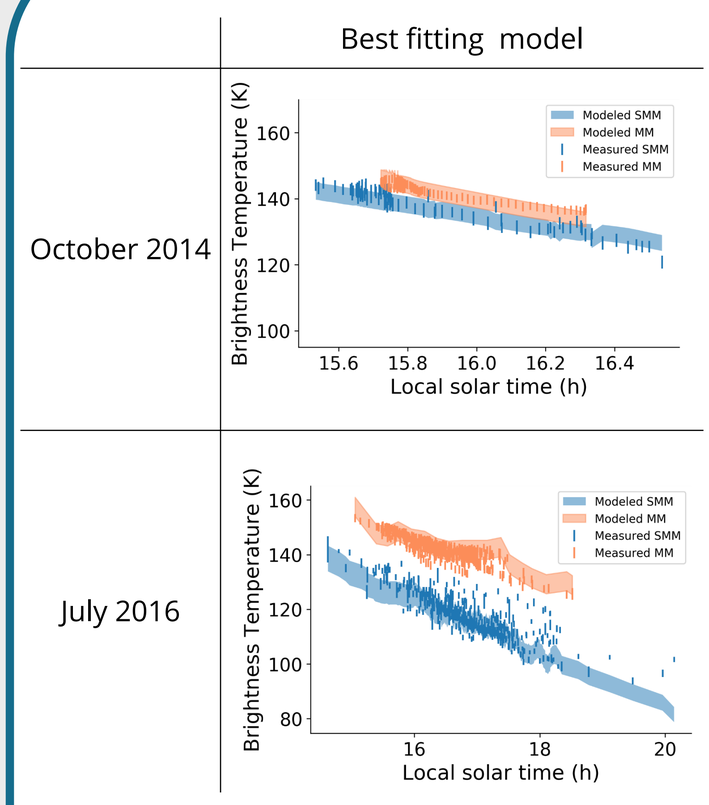


*Figure 4: Measured and modeled brightness temperatures as a function of the local solar time of the area observed. The vertical lines represent the measurements with their respective error bars and the shaded areas represents the model output.*

- Using the model described previously and making conservative assumptions on the subsurface thermal and electrical properties we were able to retrieve for each date a set of parameters that offer a good fit to the measurements.
- For both dates we have a thermally insulating porous (porosity >70%) dust layer containing little water ice (ice fraction <12%) overlaying a more compact (porosity 40-56%) dust/ice layer.
- Composition changes can be observed between the 2014 and 2016 measurements, namely the 2016 composition is more porous and contains less ice.
- As the comet passed through perihelion between the two observations these changes could be attributed to a sublimation of the water ice present in the subsurface.
- In order to determine more precisely the change in properties, and quantify the change in water ice content in the subsurface, the uncertainty on the composition must be reduced.
- This will be done by making more realistic assumptions when calculating the subsurface thermal and electrical properties.

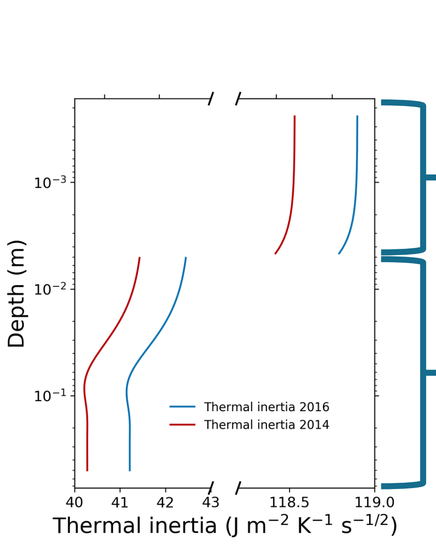


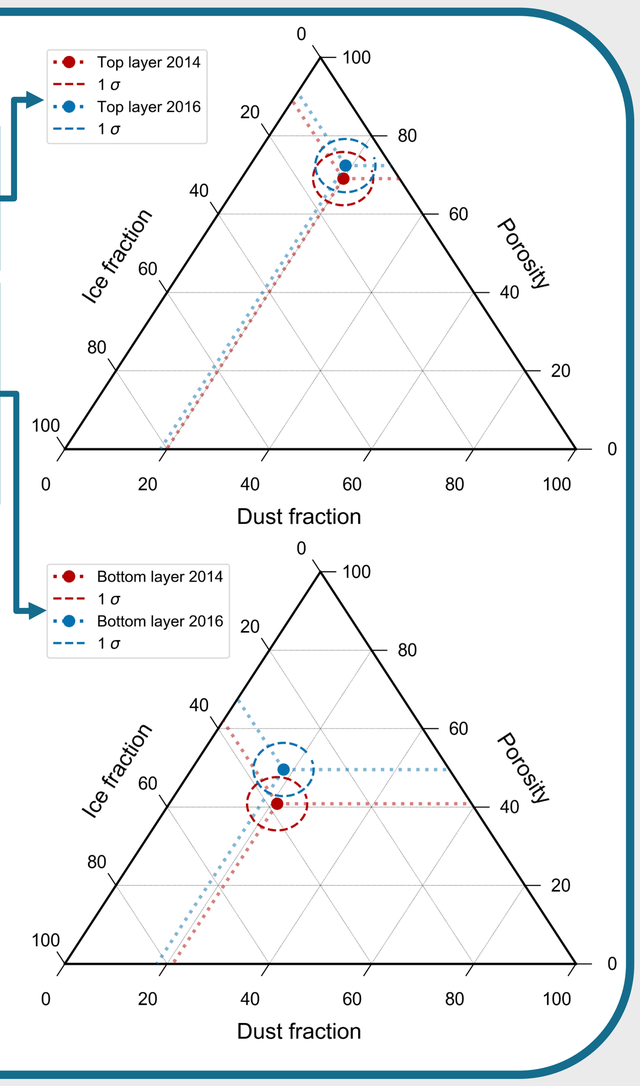


*Figure 5*

*Top: Thermal properties of the subsurface as a function of depth calculated with the best fitting parameters.*

*Top right: Ternary diagram representing the best fitting composition of the top layer for both periods of observation.*

*Bottom right: Ternary diagram representing the best fitting composition of the bottom layer for both periods of observation.*

**National Aeronautics and Space Administration**

**Jet Propulsion Laboratory**
California Institute of Technology
Pasadena, California

www.nasa.gov

**Poster No. P-03**

National Aeronautics and Space Administration

# Late-Stage Diagenetic Concretions in the Lacustrine Murray Formation, Gale Crater, Mars

**Vivian Z. Sun (3223) and Kathryn M. Stack (3223)**

## 1. Introduction

The Mars Science Laboratory (MSL) Curiosity rover has explored over 300 meters of the Murray formation (fm.) and discovered evidence for a long-lived lake at Gale crater. Numerous diagenetic features like sulfate veins and concretions have been observed and indicate that water-rock interactions occurred even after the initial deposition of the lake sediments.

Concretions are hard masses formed from mineral cement precipitation during diagenesis[1]. Martian concretions were observed previously at Meridiani Planum (hematite "blueberries"[2]) and in the Yellowknife Bay fm. at Gale[3], but the Murray fm. concretions exhibit a greater diversity of morphologies than previously observed on Mars. Here we conduct a survey of concretions throughout the Murray fm. and constrain the relative timing of diagenetic events at Gale crater.

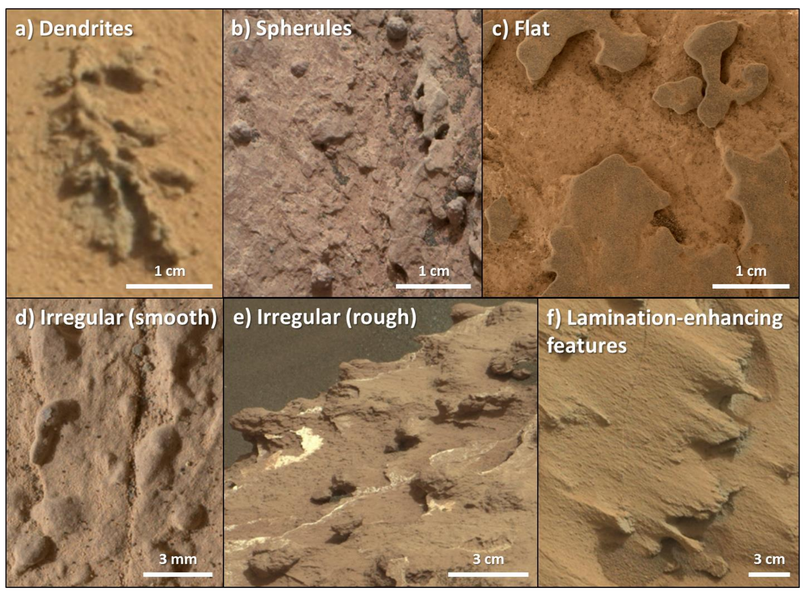


**Figure 1.** Examples of the concretion morphologies studied from Mastcam and MAHLI images in this work:

A) Dendrites (mcam03304)
B) Spherules (Spider_Lake, MAHLI 25 cm)
C) Flat concretions (Jones_Marsh, MAHLI 5 cm)
D) Smooth-textured irregular concretions (Quela postsieve, MAHLI 5 cm)
E) Rough-textured irregular concretions (mcam07703)
F) Lamination-enhancing features (mcam03423).

## 2. Concretion Distribution

Concretions are observed throughout almost the entire Murray fm. traversed from Sols 750-1900, and certain concretion assemblages (i.e. "concretion facies") are associated with particular Murray members.

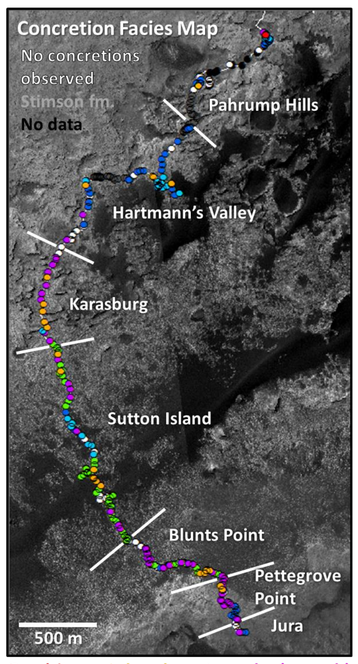


**Figure 2 (Above).** Distribution of the dominant concretion morphology observed along Curiosity's traverse.

Dendrites occur only in the basal portion of the Pahrump Hills member. Pahrump Hills and Hartmann's Valley are characterized largely by irregular concretions and lamination-enhancing features. Karasburg, Sutton Island, and Blunts Point contain a mélange of spherules, flat concretions, and irregular concretions.

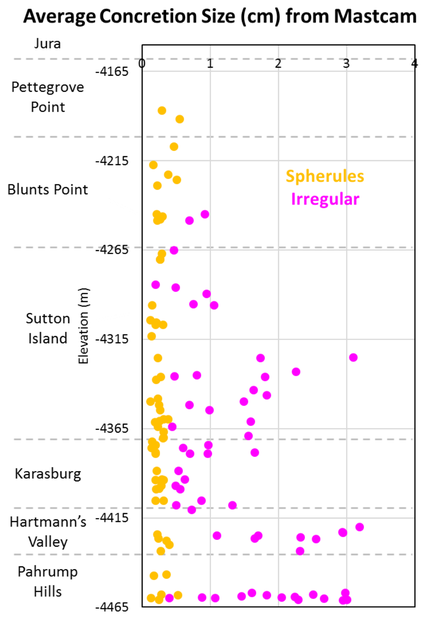


Concretion size generally decreases upsection and are smallest in Pettegrove Point and Jura, suggesting lower porosity or permeability in these Vera Rubin Ridge-forming members.

**Figure 3 (Left).** Spherule and irregular concretion size measured in Mastcam images.

## 3. Late-Stage Diagenetic Origin

The preservation of laminations within some concretion bodies suggests that most Murray concretions formed during late diagenesis after the host sediments had already been compacted and lithified. A late-stage diagenetic origin is also supported by the lack of deflected host rock lamination around concretions. However, a depositional or early diagenetic origin cannot be ruled out for some concretions.




**Figure 4.** Examples of preserved laminations within concretions.

A) Ibex_Pass (mcam03415)
B) mcam07205
C) Crowder (mcam03447)
D) Nokaneng (mcam07579)
E) mcam03455
F) mcam03405

## 4. Multiple Diagenetic Episodes

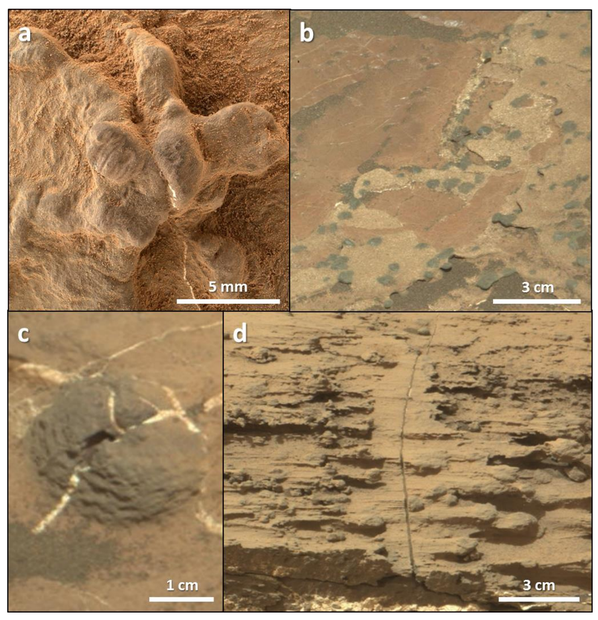


**Figure 5.** A) Positive association in dendrite Moenkopi (MAHLI 2 cm). B) Concretions enveloped in sulfate sheets (mcam09047). C) Veins crosscut concretions (mcam06673). D) Antithetical relationships (mcam07241).

Complex relationships between concretions and veins suggest that multiple diagenetic episodes occurred in the Murray fm. Concretions can be positively associated with veins, suggesting contemporaneous formation (Fig. 5a). Veins can also envelope (Fig. 5b) or crosscut concretions (Fig. 5c), suggesting vein formation postdating the concretions. Antithetical relationships suggest likely post-concretion veins that dissolve pre-existing concretions (Fig. 5d).

## 5. Diagenetic History at Gale Crater

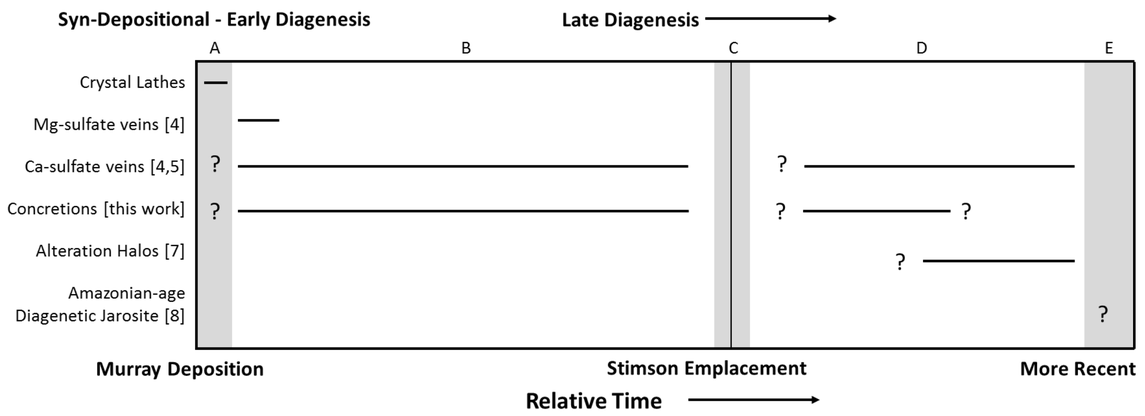


Multiple events formed the suite of Murray diagenetic features: A) Syn-depositional or early-diagenetic crystal lathes and some veins or concretions. B) Period of Mg-sulfate and Ca-sulfate vein formation[4,5] intermingled with concretion formation, extending into late diagenesis. C) Emplacement of the Stimson fm.[6] D) Post-Stimson formation of Ca-sulfate veins, concretions, and alteration halos[7]. E) Amazonian-age formation of diagenetic jarosite[8].

**Poster No. P-05**

**National Aeronautics and Space Administration**

**Jet Propulsion Laboratory**
California Institute of Technology
Pasadena, California

www.nasa.gov



**References:** [1] Seilacher, A. (2001). Sedimentary Geology, 143(1), 41–57. [2] Squyres, S. W. et al. (2004). Science, 306(5702), 1709–1714. [3] Stack K. M. et al.(2014). Journal of Geophysical Research: Planets, 119(7), 1637–1664. [4] Kronyak, R. et al., in prep. [5] Nachon, M. et al., in prep. [6] Banham, S. G. et al. (2018). Sedimentology, 65(4), 993–1042. [7] Yen, A. S. et al. (2017). Earth and Planetary Science Letters, 471, 186–198. [8] Martin P. E. et al. (2017). Journal of Geophysical Research: Planets, 122(12), 2803–2818.

National Aeronautics and Space Administration

# Surface Morphologies of Arcadia Planitia as an Indicator of Past and Present Near-Surface Ice on Mars

Author: Nathan R. Williams (3223), Matthew P. Golombek (3223)
Jet Propulsion Laboratory, California Institute of Technology

**Problem:** What is the latitudinal extent of ice on Mars, as shown by the distribution of meter-scale ice-related surface morphologies?

## Introduction

- Surface water is in disequilibrium with atmosphere today at low- and mid-latitudes[1,2], yet a latitude-dependent mantle of shallowly buried water-ice occurs from polar caps down to the mid-latitudes, with several lines of supporting evidence:
  - Neutron spectrometer detects ~35% ice by weight[3]
  - Ground-penetrating radar shows reflectors at 20-80 m depths with dielectric constants similar to ice[4,5]
  - Near-surface ice revealed in situ by the Phoenix lander (68°N, 234°E)[7,8]
  - Polygonal patterned ground[9]
  - Small, fresh impacts eject bright ice from <1m depth[6]
  - Sublimation expanded secondary crater diameters[10]
  - Terraced craters suggest a mechanical discontinuity ~50m deep[5]
  - Lobate debris aprons[4,11]
- Arcadia Planitia at approx. 40°N, 200°E, -4 km elevation, has some of the most equatorward ice deposits with these features
- However, all of the above methods have coarse resolutions or sparse sampling that limits mapping the extent of ice

## Methodology

- We surveyed 230 HiRISE images at ~25 cm/pixel[12] from 185°E to 210°E and 35°N to 44°N, and identified ice-related surface morphologies present:
- Polygonal patterned terrain consists of gentle mounds bounded by ridges or troughs, is interpreted as ice-cemented substrate undergoes solid state convection or ice wedging[7-9]

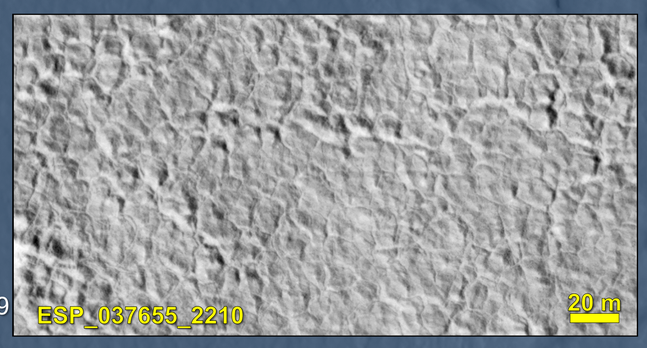


- Crenulated or “brain coral” terrain consists of sinuous troughs and ridges, hypothesized to form by thermal contraction cracking and differential sublimation[13,14]

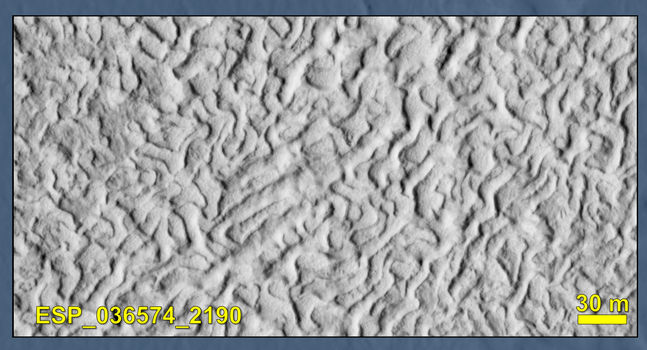


- Pitted terrain, consisting of scattered shallow depressions, likely represents localized sublimation along thermal contraction fractures

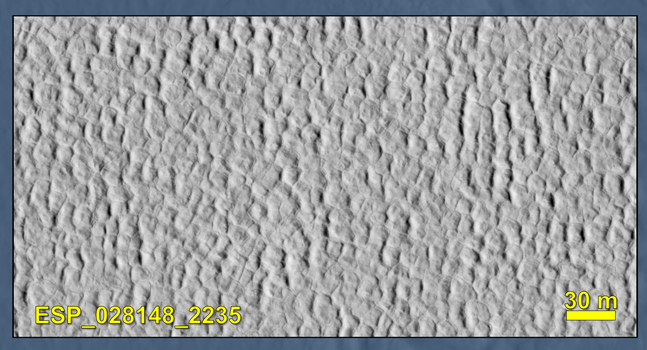


## Results

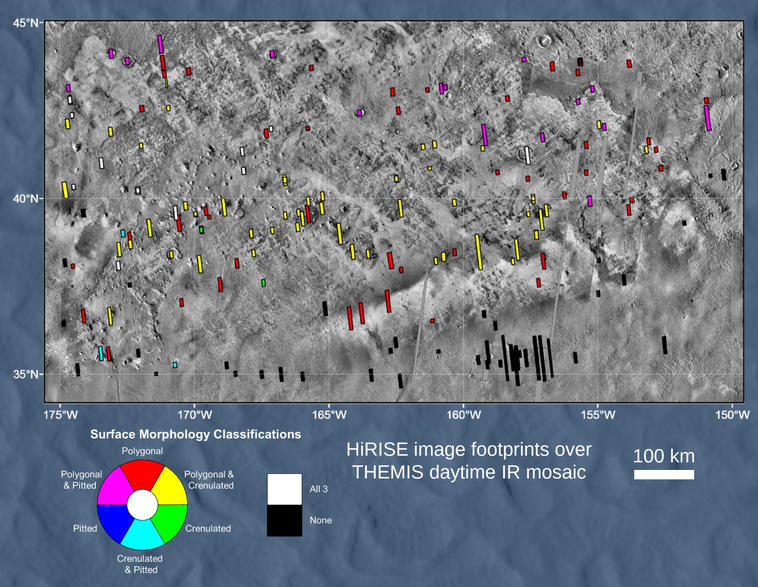


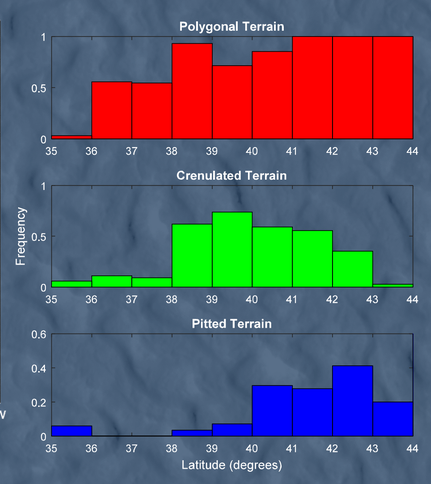


- Polygonal terrain is ubiquitous poleward of 41°N, progressively becomes less common from 41°N to 36°N, and is scarce equatorward of 36°N
- Crenulated terrain primarily occurs in a narrow latitude band between 38°N and 43°N
- Pitted terrain primarily occurs >40°N and is typically associated with polygons

## Interpretations and Implications

- The latitude-dependent transition in morphology from pits to crenulations that progressively degrade southward indicates meters-thick ice is still present >38°N, but is sublimating away
- Polygonal surface patterns indicate the recent presence of ice across a wide range of latitudes, but polygons also fade towards the south (esp. <38°N) where they represent mostly desiccated terrain with relatively little to no excess ice remaining
- The present-day edge of the latitude-dependent mantle of shallow ice is between ~38°N and ~40°N in Arcadia Planitia
- Arcadia Planitia’s large ice deposits are some of the closest to the equator and a priority for future use as an in-situ resource

## References

We gratefully acknowledge the HiRISE science and engineering teams for creating the superb image dataset used in this project.

[1] Head J. W. et al. (2003) *Nature*, 426, 797-802. [2] Bramson, A. M. *et al*. (2017) *LPSC*, 48, 2692. [3] Boynton W. V. et al. (2002) *Science*, 297, 81-85. [4] Plaut J. J. et al. (2009) *Geophys. Res. Lett*., 36, L02203. [5] Bramson A. M. et al. (2015) *Geophys. Res. Lett*., 42, 6566-6574. [6] Byrne S. et al. (2009) *Science*, 325, 1674-1676. [7] Arvidson R. E. et al. (2009) *JGR*, 114, E00E02. [8] Mellon, M. T. et al. (2009) *JGR*, 114, E00E06. [9] Levy J. et al. (2009) *JGR*, 114, E01007. [10] Viola D. et al. (2015) *Icarus*, 248, 190-204. [11] Mangold N. (2003) *JGR*, 108, 1885. [12] McEwen A. S. et al. (2007) *JGR*, 112, E05S02. [13] Dobrea, E. N., *et al*. (2007) *7th Intl. Conf. on Mars*, 3358. [14] Levy J. S. et al. (2009) *Icarus*, 202, 462-476.

**National Aeronautics and Space Administration**

**Jet Propulsion Laboratory**
California Institute of Technology
Pasadena, California

www.nasa.gov



**Poster No. P-06**

National Aeronautics and Space Administration

# Eris: The brightest (and most active?) Kuiper belt object

**Jason D. Hofgartner (JPL Group 3224), Bonnie J. Buratti (3224), Paul O. Hayne[1], Leslie A. Young[2]**

1. Department of Astrophysical and Planetary Sciences, University of Colorado, Boulder, CO; 2. Southwest Research Institute, Boulder, CO;

## 1. Eris 101

Eris is a large Kuiper belt object (KBO) that is similar to Pluto in several of its bulk properties.

| | |
|---|---|
| Orbit | 38 – 98 AU, 557 year period<br>Aphelion in 1977 and presently 96 AU from Sun |
| Mass and Radius | 1.27 and 0.98 mass and radius of Pluto respectively |
| Visible Geometric Albedo | 0.96, highest of any known KBO |
| Volatiles | Nitrogen and methane with bulk abundances of 9 $N_2$ : 1 $CH_4$ |
| Satellites | One known: Dysnomia |
| Spin and Obliquity | Unknown and unknown<br>If tidally locked to Dysnomia: 16 days and 78$^O$ with current subsolar latitude of 40$^O$ |

## 2. Motivation: High Albedo Implies Activity

Eris is exceptionally bright with a visible geometric albedo of ~0.96 (Sicardy+ 2011), greater than any other known KBO. Its infrared reflectance spectrum is dominated by methane (Brown+ 2005), which should form tholins that darken the surface on timescales much shorter than the age of the solar system (Stern+ 1988). Thus one or more ongoing processes probably resupply methane and maintain its surface brightness.

Atmospheric freeze-out (collapse onto the surface) as Eris recedes from its perihelion distance of 38 AU to 98 AU at aphelion is a prevalent hypothesis to explain its anomalous albedo (e.g., Brown+ 2005; Sicardy+ 2011).

## 3. Global and Local, Collisional, Sublimation Atmospheres

**Sublimation atmosphere:** Primary constituent is in vapor pressure equilibrium (VPE) with frost on the surface.

**Collisional atmosphere:** Vapor particles interact with each other and do not follow ballistic trajectories.

**Global, collisional, sublimation atmosphere:** Approximately uniform pressure everywhere around the globe (isobaric); VPE implies uniform frost temperature (isothermal). Mars, Triton, & Pluto have this type of atm.

**Local, collisional, sublimation atmosphere:** Condensation and/or sublimation rates exceed the rate of atmospheric transport and atmospheric transport cannot maintain a globally uniform pressure. The temperature of the frosts are not held isothermal by VPE with an isobaric atmosphere. A local atmosphere occurs over the warmest (~subsolar) frost covered region but the atmospheric pressure decreases over colder frosts away from this region. The pressure gradients generate winds that transport the volatile away from the warmest region. Due to the significant decrease in pressure away from the warmest region, the transport may not include the whole globe. Io has this type of atmosphere and several other KBOs are also predicted to have this type of atmosphere (Young and McKinnon 2013).

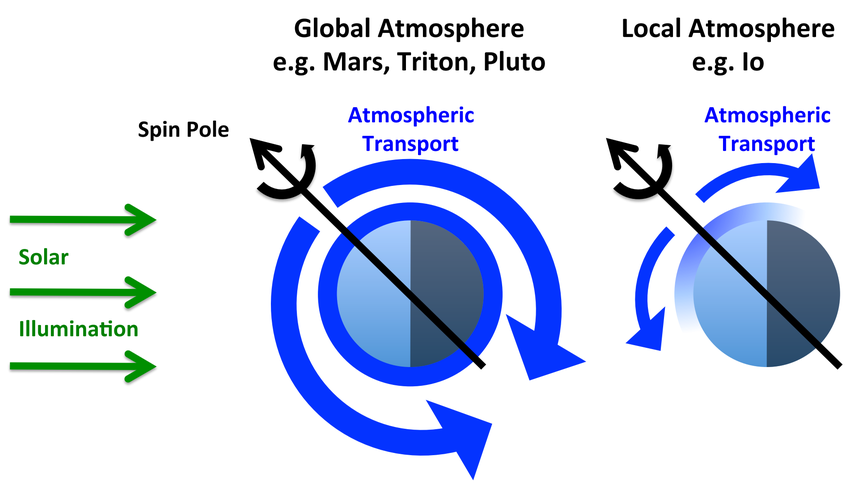


We define $\alpha$ as the ratio of the timescale for atmospheric freeze-out to the timescale for communicating pressure changes (pole-to-pole distance divided by the sound speed). We define $\beta$ as the ratio of the pressure scale height to the mean free path. These $\alpha$ and $\beta$ parameters correctly predict whether the sublimation atm. is global or local and collisional or ballistic for Mars, Io, Triton, and Pluto.

| | $\alpha$ | $\beta$ |
|---|---|---|
| **Mars** | 20 | 1 x $10^9$ |
| **Io** | 3 x $10^{-5}$ | 200 |
| **Triton** | 90 | 2 x $10^7$ |
| **Pluto** | 200 | 3 x $10^7$ |
| **Eris (perihelion, albedo = 0.1 - 0.9)** | 2000 – 0.008 | 7 x $10^8$ - 200 |
| **Eris (aphelion, albedo = 0.1 – 0.9)** | 0.1 – $10^{-11}$ | 3 x $10^3$ – 8 x $10^{-8}$ |

Eris's eccentric orbit is expected to result in two atmospheric regimes: (1) a period near perihelion when the atmosphere is global and (2) a period near aphelion when only a local atmosphere exists near the warmest (~subsolar) region. In both regimes the atmosphere is collisional (not ballistic) and maintained by VPE.

## 4. Coupled Thermal-Transport Numerical Model of Local, Collisional, Sublimation Atmospheres

Volatile transport in the global, collisional, sublimation atmosphere regime has been modeled with a numerical thermal model that conserves energy and mass while maintaining VPE (e.g., Leighton and Murray 1966; Hansen and Paige 1992; 1996). These models assume a uniform pressure which implicitly incorporates transfer of energy and mass, so these models do not explicitly track the atmospheric transport.

Volatile transport in the local, collisional, sublimation atmosphere regime has been modeled with a meteorological model that conserves energy, mass, and momentum (Ingersoll+ 1985). The model prescribed the frost temperature distribution, did not include latent heat, and assumed symmetry about the subsolar/antisolar axis. As a result, both the thermal and temporal behavior were not explicitly modeled.

We combine elements of the two types of models discussed above to model the local, collisional, sublimation atmosphere regime with a coupled thermal-transport numerical model that conserves energy, mass, and momentum while maintaining VPE. This model does not include any of the assumptions noted above and thus is not subject to the same limitations and can be adapted to any body with a local, collisional, sublimation atmosphere.

## 5. Results: Significant Volatile Transport

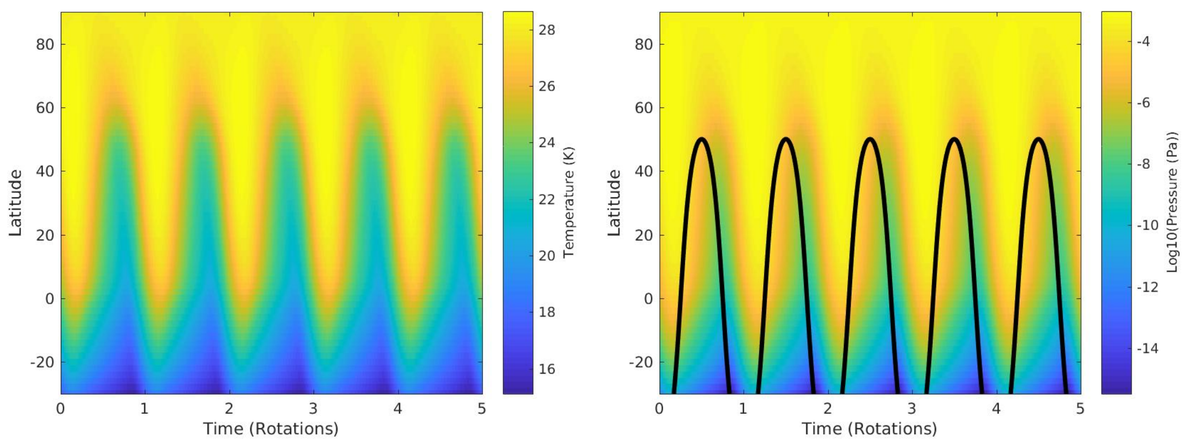


Example results for Eris of the coupled thermal-transport numerical model. Left panel: frost temperature, there is a diurnal oscillation, the maximum is near the subsolar latitude (40$^O$) shortly after local noon, and the values are comparable to the planetary equilibrium temperature (~23 K). Right panel: vapor pressure. The pressure of the atmosphere at the surface is constrained by a stellar occultation to be < $10^{-4}$ Pa (1$\sigma$ confidence level) over the limb of the disk but could be greater away from the limb (Sicardy+ 2011). The black lines indicate the limb. The predicted pressures at the limb are consistent with the upper limit.

This example demonstrates that the model results are reasonable and are testable predictions.

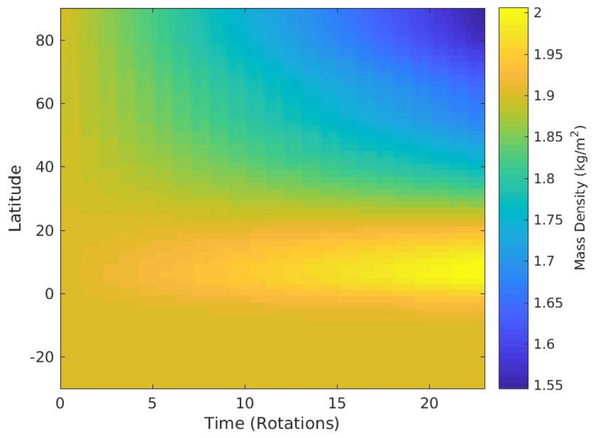


The plot to the left shows the frost mass per unit area for 23 rotation periods (~1 Earth year). The initial frost mass is everywhere equal to the precipitable column of nitrogen in Pluto's atmosphere during the New Horizons encounter (the resultant frost if the Pluto atmosphere collapsed uniformly over the globe). Eris is held at its aphelion distance, where the incident solar flux is a minimum, as a limiting case. After one year the pole has lost an appreciable amount (~20%) of nitrogen frost to the equator. In this simulation the pole of Eris is frost free after < 6 years. Thus even for the extreme limiting case of aphelion and assuming reasonable thermal parameters, volatile transport on Eris can significantly alter the surface on decadal timescales.

## 6. Conclusions

1. Developed coupled thermal-transport model for local, collisional, sublimation atmospheres
   - Applicable to Eris, other KBOs with local, collisional, sublimation atmospheres, and Io
2. Local atmosphere on Eris can transport significant (as compared to Pluto atmosphere) mass and energy
   - Even at ~100 AU solar distance, with surface temperatures < 30 K and vapor pressures < 1 nbar
   - Although Eris is 96 AU from the Sun in 2018, volatile transport may result in changes in albedo and/or color that are observable with Earth-based telescopes
3. Uniform condensation of a Pluto-like atmosphere likely cannot explain Eris's high albedo
   - Seasonal volatile transport in general is still a plausible hypothesis
   - Other geologic processes such as convection and glaciation that are now thought to be the primary processes renewing Pluto's brightest regions (e.g., McKinnon+ 2016; Moore+ 2016) are also plausible

**National Aeronautics and Space Administration**

**Jet Propulsion Laboratory**
California Institute of Technology
Pasadena, California

www.nasa.gov



Acknowledgements: Jason Hofgartner was supported by an appointment to the NASA Postdoctoral Program administered by Universities Space Research Association through a contract with NASA. This work was inspired by the New Horizons exploration of Pluto.

**Poster No. P-07**

National Aeronautics and Space Administration

# Can Earth-like plate tectonics occur in the outer ice shells of icy satellites?

**Author: Samuel M. Howell (3225)**

**Robert T. Pappalardo (3204)**

## 1. Background and Motivation

The outer $H_2O$ ice shells of some icy satellites show evidence for divergent, strike-slip, and convergent tectonics. Researchers thus propose that Earth-like plate tectonic processes may occur in the ice shells of Europa and Enceladus (Bland and McKinnon, 2017; Johnson et al., 2017; Kattenhorn and Prockter, 2014), raising the possibility of a buoyantly driven cycle of tectonic resurfacing and lithosphere recycling on icy satellites.

Such a cycle could quickly deliver oxidants produced on the surfaces of outer ice shells to reductants produced on the seafloors of interior water oceans, sustaining redox gradients at a rate that may be necessary for life to originate or persist (Hand et al., 2007; Russell et al., 2014; Vance et al., 2016). Johnson et al. (2017) recently demonstrated that a subducting ice I slab on Europa may remain negatively buoyant for appropriate values of salt content, salt distribution, and porosity of the subducting plate, providing a mechanism for slab pull in the case where other forces allowed the initial formation of an convergent margin. Thus, understanding the mechanism that drives observed tectonic resurfacing on these bodies and the associated timescales of surface-ocean interaction has fundamental implications for the habitability of icy satellites and the ability of spacecraft to detect signs of interior life at the surface.


Subduction could sustain redox gradients in the ocean and drive tectonics

To explore whether Earth-like, convectively driven plate tectonics can occur in the outer shells of icy satellites, we adapt a simple force balance to determine whether buoyancy forces can initiate or sustain subduction on Europa, Enceladus, Ganymede, and Triton. This spans the smallest to the largest icy satellites with pervasive surface tectonics over a range of inferred ice shell thicknesses. As a feasibility test, we incorporate the most optimistic first-order assumptions, promoting Earth-like plate tectonics to the greatest possible extent.

## 2. Force Balance Method

**For subduction to occur, the driving forces must overcome the resisting forces.**

In the analog model to the right, a rock hammer is negatively buoyant compared to an empty aloe water bottle. The hammer does not "subduct" into the bottle because the inherent mechanical strength of the bottle is greater than the force provided by the negative buoyancy of the hammer.


3 kg hammer with 3 cm² contact area ~100 kPa
(~ diurnal tidal stress on Europa)
(Exerted by ~3 km of subducting slab, @ $\Delta\rho$=40 kg/m³)

Yield Strength of HPDE is 15 MPa
(~ 10 km thick Europa lithosphere)
(Exerted by ~400 km of subducting slab @ 40 kg/m³)

### Driving and resistive forces

Slab Pull, $F_S$
*The negative buoyancy force of a subducting slab*

Ridge Push, $F_R$
*The outward push of a perched, buoyant band*

Subduction Zone Frictional Strength, $F_F$
*The internal mechanical strength of the interface*

Elastic Bending, $F_E$
*The force required to bend the slab at the interface*

### Schematic of subduction parameters

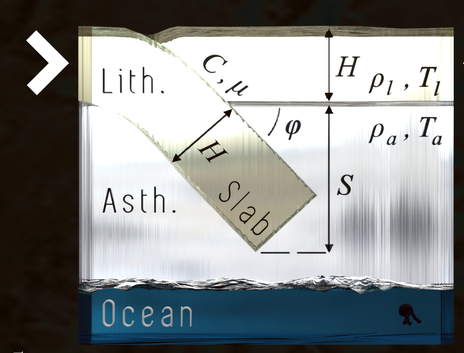


$$(\rho_l - \rho_a)\, gSH + \tfrac{1}{2}\rho_a g w H > \frac{CH + \tfrac{1}{2}\mu\rho_l g H^2}{\sin\theta\cos\theta - \mu\sin^2\theta} + \frac{1}{12}\eta u$$

($\rho_l$: slab/plate density; $\rho_a$: interior density; $g$: gravity; $S$: slab depth; $H$: plate thickness; $w$: band height; $C$: cohesion; $\theta$: fault dip; $\mu$: friction coef.; $\eta$: plate visc.; $u$: convergence rate)

## 3. Force Balance Results

### Comparison of force magnitudes for increasing fraction of total ice shell penetration

Resistive forces required to bend the lithosphere, $F_E$, and overcome subduction zone friction, $F_F$, and driving buoyancy forces from slab pull, $F_S$, and ridge push FR.

Ratio of the mechanical forces resisting subduction to the buoyant forces driving subduction,

$$(F_E + F_F) / (F_S + F_R)$$

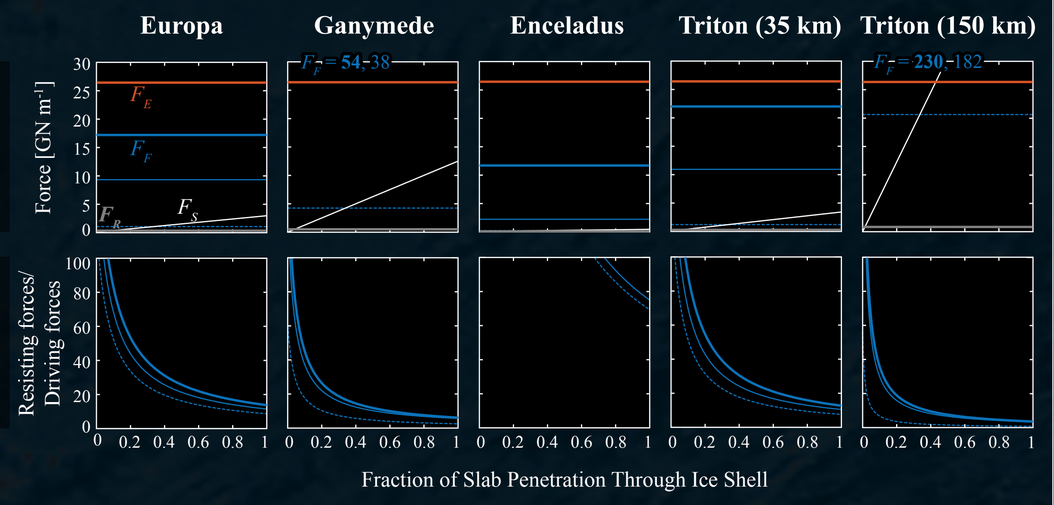


Pristine ice shell (C = 1 MPa, μ = 0.6)
Established subduction zone (C = 100 kPa, μ = 0.6)
Pervasively damaged, nearly frictionless subduction zone (C = 0, μ = 0.1)

### Subduction requirements for increasing fraction of total ice shell penetration

The density contrast between the downgoing slab, $\rho_l$, and the interior ice asthenosphere, $\rho_a$, required for subduction. The white line shows a predicted contrast.

The "missing" regional stress required in addition to buoyancy stresses in order for subduction to occur.

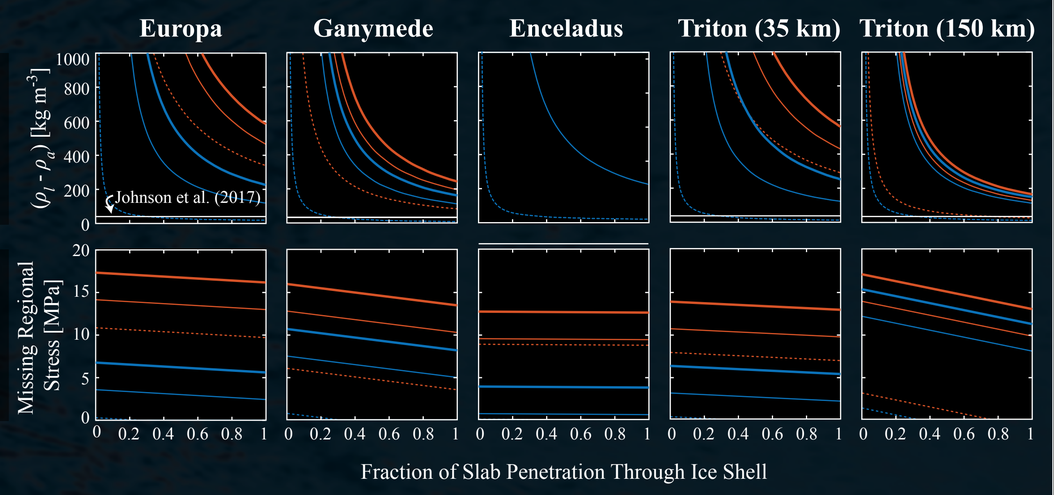


Force required to bend the lithosphere and overcome the frictional strength of the subduction zone, $F_F$+$F_E$

Force required to only overcome the frictional strength of the subduction zone, $F_F$

## 4. Impact and Importance

### Conclusions

**The mechanical resistance opposing subduction is of significantly higher order than the buoyancy forces driving subduction.** Any buoyancy permanently present within a downgoing slab is unlikely to contribute significantly to tectonic forcing on any icy satellite.

**Despite numerous optimistic assumptions, driving tectonics through thermo-chemical convection requires a remarkably weak ice shell or unrealistic compositional contrast.** We ignore drag between the plate and interior, slab porosity, and the loss of thermal and compositional density to advection, diffusion, conduction, and convection. We estimate the mechanical and elastic lithosphere as being very thin, and use conservatively low convergence rates.

**The timescale of material delivery from the surface is not likely to be controlled by the relatively fast convective timescale of tens-to-hundreds of kyr (e.g. Howell and Pappalardo, 2018).** The seafloor may go without surface material delivery for many hundred thousand to tens-of-millions of years if ice shell rotation or ice shell thickening drive convergence.

### Relevance to proposed and ongoing missions

Future missions to the outer ice shells of icy satellites, including the planned NASA Europa Clipper and ESA Juice missions, and proposed NASA Europa lander, should consider the possibility that **present-day surface material may not be indicative of the present-day ice shell interior or ocean composition.**

Further, missions geared towards the future detection of possible life within these bodies should consider how the slow or periodic delivery of surface material, occurring over $10^5$ to $10^8$ years might affect the potential habitability of icy satellite oceans. **Instrument requirements for life detection missions should consider the possibility of limited surface-interior exchange when evaluating the detection limits for potential biomaterials.**

**National Aeronautics and Space Administration**

**Jet Propulsion Laboratory**
California Institute of Technology
Pasadena, California

www.nasa.gov



**Poster No. P-08**

National Aeronautics and Space Administration

# Preservation of potential biosignatures on Europa's surface


## Author: Tom Nordheim (3225) Advisor: K.P. Hand (3204)


Accurate knowledge of Europa's surface radiation environment is essential to the interpretation of space and Earth-based observations of Europa's surface and exosphere. Furthermore, **future landed missions may seek to sample endogenic material emplaced on Europa's surface to investigate its chemical composition and to search for biosignatures contained within**. This material would likely be sampled from the shallow sub-surface, and thus, **it is crucial to know to which degree surface material is expected to have been radiation processed.**

Here **we present modeling results for energetic electron and proton bombardment of Europa's surface**, including interactions between these particles and surface material.

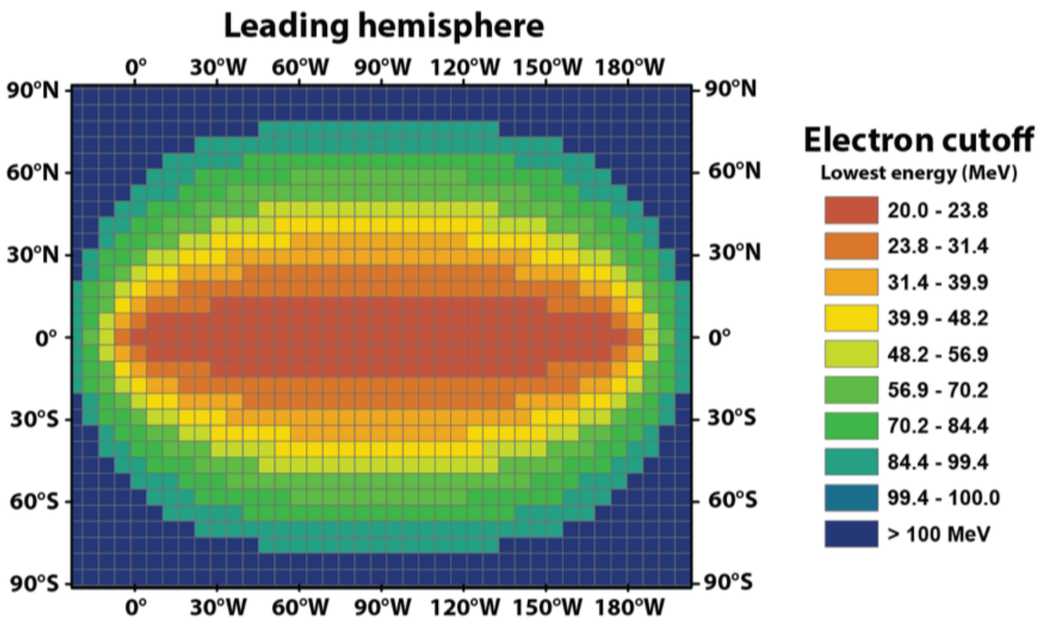


**Figure 1: Electron bombardment patterns for Europa's leading hemisphere**

At the **leading hemisphere (above),** the cut-off energy represents the **lowest** energy electrons within the 20 – 100 MeV range that can reach that location.

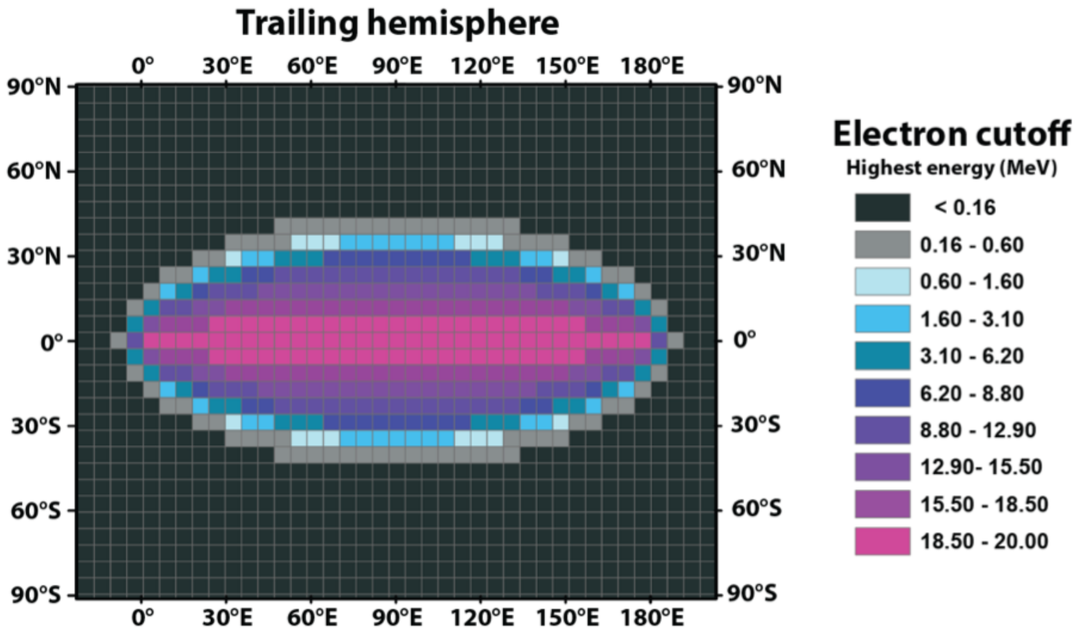


**Figure 2: Electron bombardment patterns for Europa's trailing hemisphere**

At the **trailing hemisphere (above),** the cut-off energy represents the **highest** energy electrons within the 10 keV – 20 MeV range that can reach that location.


**National Aeronautics and Space Administration**
**Jet Propulsion Laboratory**
California Institute of Technology
Pasadena, California

www.nasa.gov




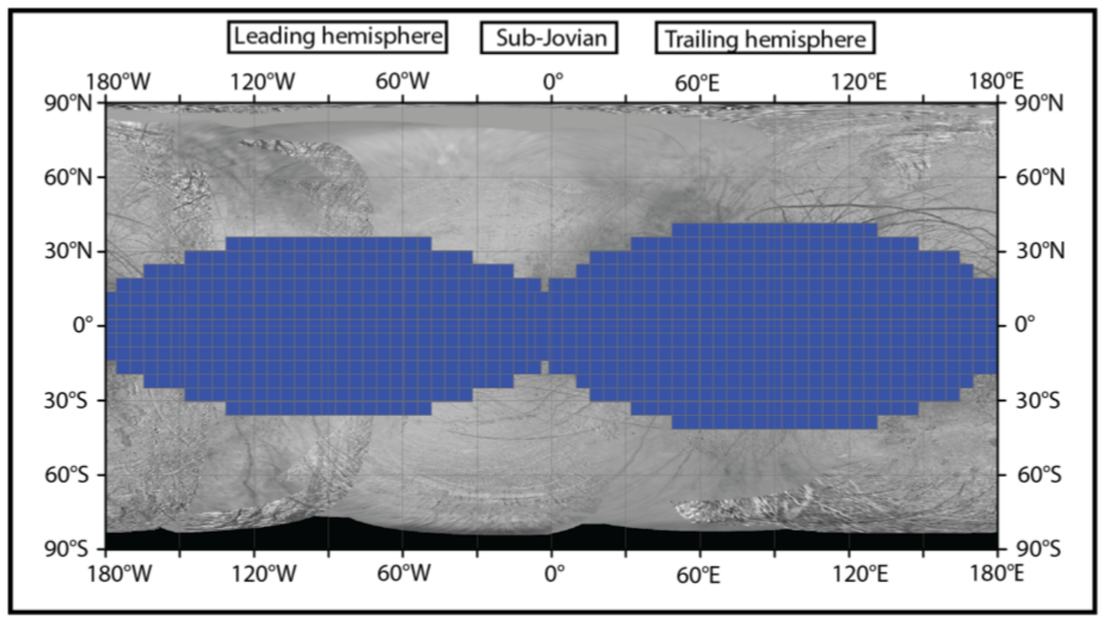


**Figure 3: Radiation processing map of Europa's surface. Locations where radiation has processed material to at least 10 cm are shown in blue.**

Our results show that there are large (order of magnitude) differences in the radiation dose rate at different geographic surface locations. **The most irradiated surface material can be found within 'radiation lenses' that are centered on the leading and trailing hemispheres**. Surface material within these regions can be expected to be radiation processed down to ~10-20 cm. **The radiation dose rate outside of these radiation lenses is over an order magnitude lower**, and surface material there is only radiation processed down to depths of a few cm.

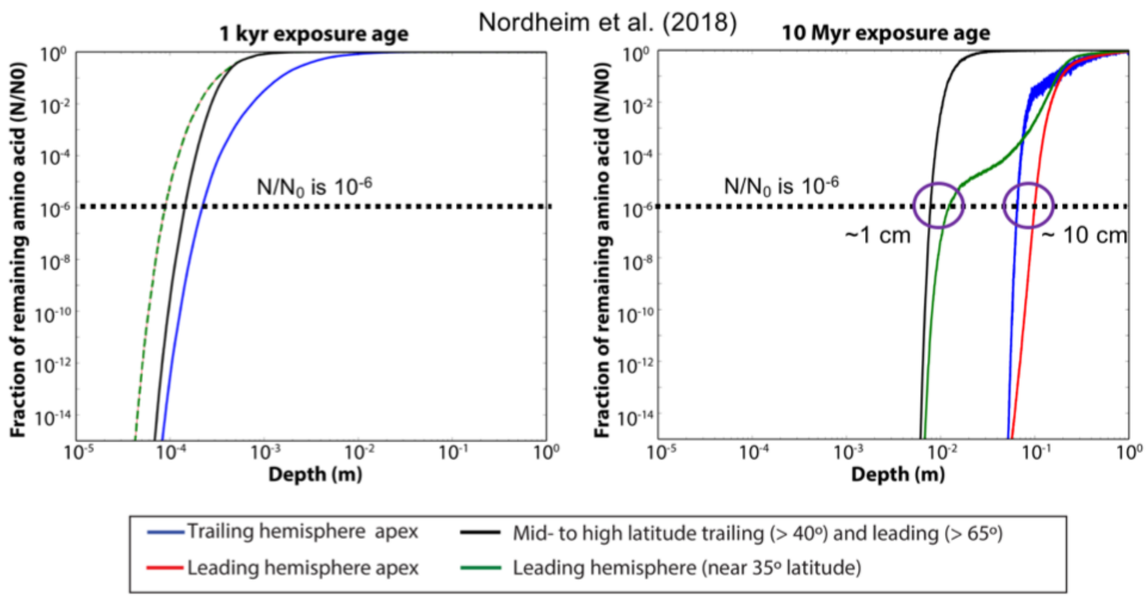


**Figure 4: Destruction of biomarkers (amino acids) within surface material for young (left) and old (right) surface material. Theoretical detection thresholds from Kminek & Bada (2006) are shown for reference (dotted lines). The quantity on the y axis ($N/N_0$) represents the fraction of amino acid remaining after the radiation dose sustained over that timescale.**

Amino acids are some of the simplest molecules that qualify as a potential biosignature. Here we have considered amino acids as a case study for biosignature destruction on Europa. **Outside of the radiation lenses, amino acids are well preserved at depths of a few cm.** We have also shown that, while heavily reduced in concentration, **amino acids persist at detectable levels at 10 cm depths even in the most harshly irradiated locations on Europa.** Amino acids contained within young (< 10 Myr) surface material on Europa is well preserved within the upper few mm at all locations.. **Future surface missions may therefore wish to sample material from locations at mid- to high latitudes and geologically young regions**

**Poster No. P-09**

National Aeronautics and Space Administration

# Quantified DUV Raman Analysis for Life Detection

**Joseph Razzell Hollis (3225-Affiliate), Haley Sapers (3225-Affiliate), Marc Fries (JSC), Rohit Bhartia (3225), Luther Beegle (3200)**

## Introduction

SHERLOC (**S**canning **H**abitable **E**nvironments using **R**aman and **L**uminescence of **O**rganic **C**ompounds) is an arm-mounted deep UV Raman/Fluorescence spectrometer selected for the upcoming Mars 2020 rover. DUV Raman spectroscopy is a powerful technique for detecting and identifying complex organic compounds based on their molecular vibrations and thus has great potential for detecting life.[1]

In order to exploit that potential, we must understand how to interpret the DUV Raman spectra of mixed organics. We will examine the spectra of two very different biosignatures: complete cells of *E. coli* and carbonaceous material produced by long-term geothermal heating of organic compounds.

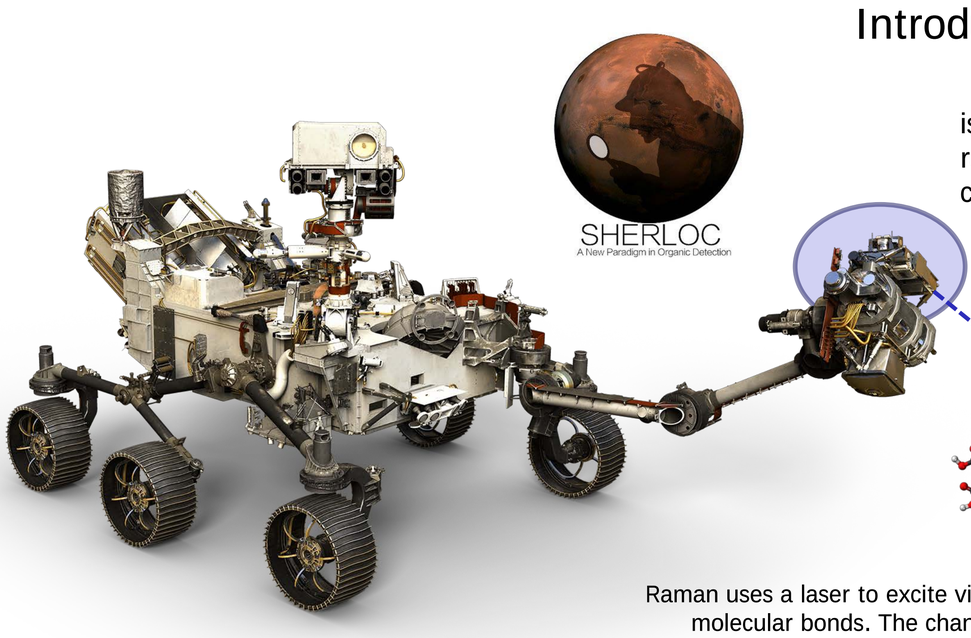


Raman uses a laser to excite vibrations of molecular bonds. The change in *E* for scattered light reveals the frequency of vibration, specific to that molecule.

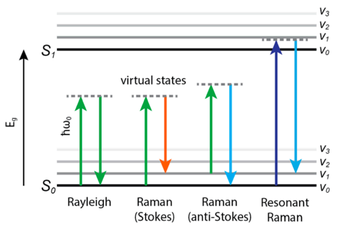


## Deconvolution of a cell's spectrum

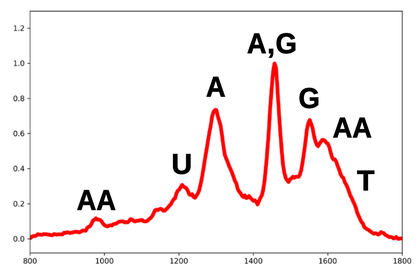


Even a simple cell contains thousands of different proteins and complex molecules, including DNA. But under DUV excitation, the Raman spectrum of *e. coli* is dominated by **resonance** with its simplest aromatic components:

**3** amino acids and **5** nucleic acids.[3]

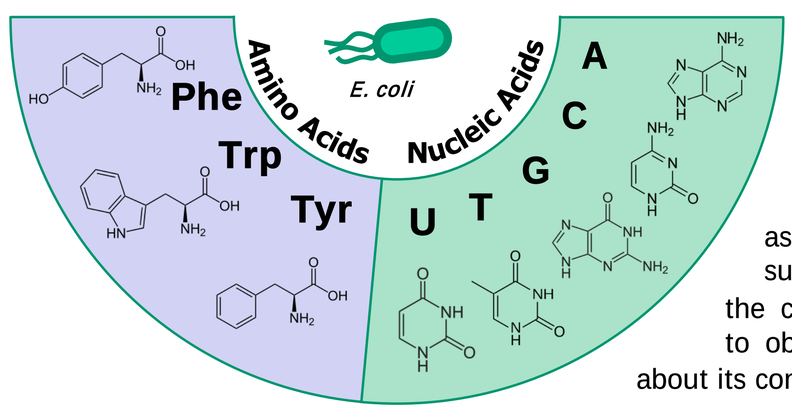


These molecules are actually present within far more complicated chemical structures, and as such we need to find a suitable model to describe the cellular spectrum in order to obtain valuable information about its components.

## Data Processing

Spectra were averaged over 9+ points across each sample, and background signal subtracted using a linear baseline. Due to instrumental variation, we recalibrated each spectrum based on the position of the atmospheric $\mathbf{N_2}$ peak, correcting to a standard value of ~2321 $cm^{-1}$

The recalibration ensured a consistent peak position between spectra taken at different times, as shown by 'old' and 'new' spectra of the simple nucleic acid *adenine*, taken 18 months apart.

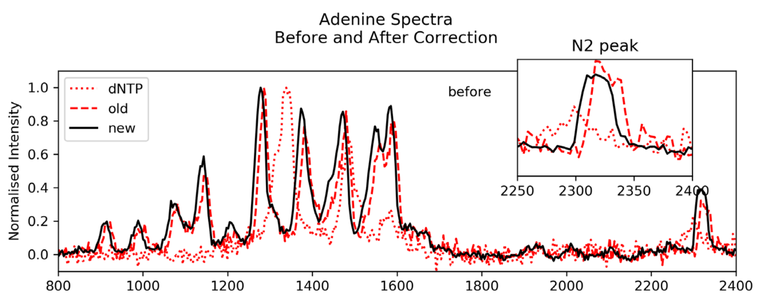


After recalibration, the atmospheric $\mathbf{N_2}$ and $\mathbf{O_2}$ peaks (at 2321 and 1550 $cm^{-1}$) were subtracted to avoid overlap with key organic peaks.

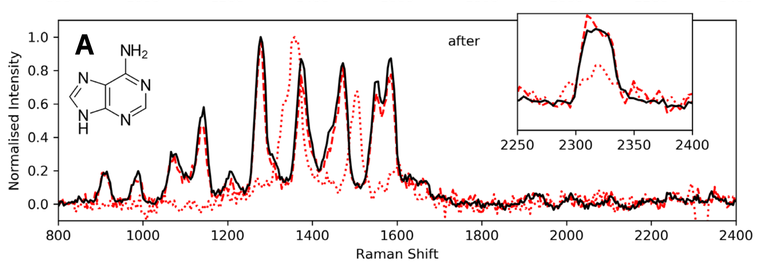


Deconvoluting the cell spectrum with the most basic forms of the **nucleic acids** resulted in a **very poor** fit, lacking the major **A** and **G** peaks at 1300, 1440 $cm^{-1}$.

The simple nucleic acids are too dissimilar to their analogues within the cell.

The more complex **nucleotides** showed fewer peaks, due to vibrational coupling between the nucleic acid and ribose moieties. These peaks line up well with their cellular analogues and produce a **much better** fit.

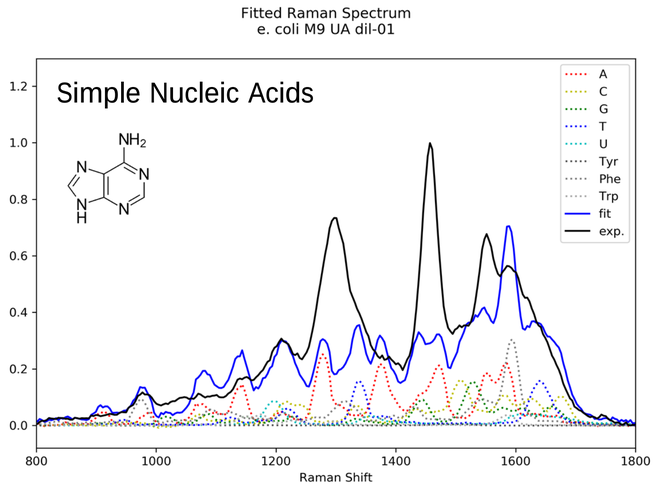


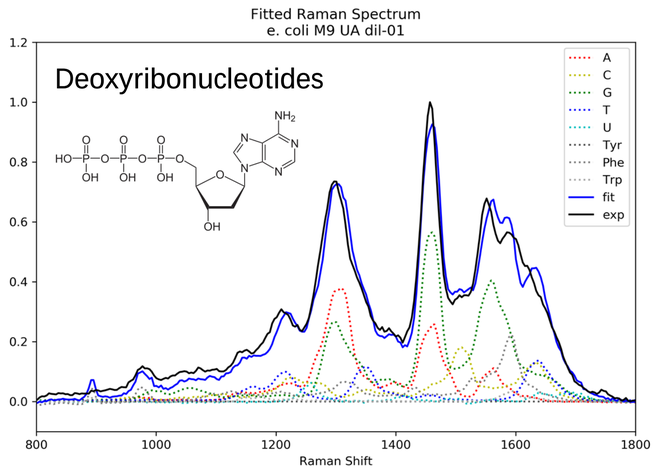


### Relative Raman Contribution

| NAs | 84% | AAs | 16% |
|---|---|---|---|
| dATP | 24% | Phe | 0% |
| dCTP | 11% | Trp | 14% |
| dGTP | 36% | Tyr | 2% |
| dTTP | 9% | | |
| UTP | 4% | | |

## Carbonaceous Material

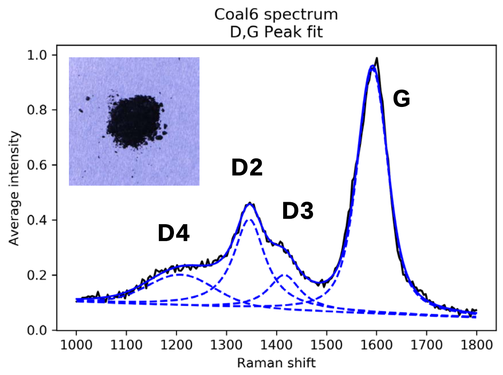


We fitted the spectrum to obtain the **D/G** intensity ratio and individual peak parameters like full-width-half-maximum.

Across 47 samples of different coals with varying rank, **D/G** ratio and **G** band FWHM decreased with increasing temperature, based on loss of N, O, S atoms due to outgassing. We conclude that heating allows organic molecules to reorganize into graphite-like lattices with a narrow range of vibrational frequencies, removing heteroatoms in the process.

Long-term geothermal non-oxidative heating of organic deposits converts organic compounds into carbonaceous materials rich in Raman-active polyaromatics, similar to coal.[2]

Coals exhibit a distinctive Raman spectrum with a sharp **G** band from highly-ordered, graphite-like carbon, and multiple **D** bands associated with disordered carbon.

Under DUV excitation, the **G** band is resonant and dominates the spectrum vs visible–light excitation. The **D2,3,4** bands are non-resonant and the **D1** band at 1650 $cm^{-1}$ isn't observed at all.

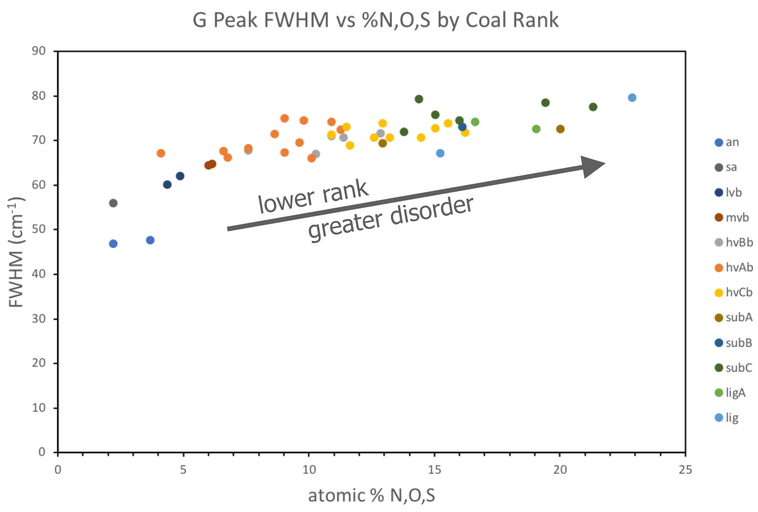


## Conclusions

The Raman spectrum of *E. coli* can be deconvoluted using standard spectra of nucleotides and amino acids in solution to find their relative intensities. Calculation of true concentrations will require measurement of Raman scattering cross-sections for each molecule of interest.

For more homogeneous samples of carbonaceous material, Raman fitting of the disordered/graphitic carbon modes can provide useful information that correlates to chemical composition and thus geothermal history.

1. Beegle, L.; *et al.* SHERLOC: Scanning Habitable Environments with Raman & Luminescence for Organics & Chemicals. In *IEEE Aerospace Conference Proceedings*; 2015; Vol. 2015–June.
2. Rahl, J. M.*; et al.* Raman Spectroscopic Carbonaceous Material Thermometry of Low-Grade Metamorphic Rocks: Calibration and Application to Tectonic Exhumation in Crete, Greece. *Earth Planet. Sci. Lett.* **2005**, *240* (2), 339–354.
3. Wu, Q.; *et al.* UV Raman Spectral Intensities of E. Coli and Other Bacteria Excited at 228.9, 244.0, and 248.2 Nm. *Anal. Chem.* **2001**, *73* (14), 3432–3440.

**National Aeronautics and Space Administration**
**Jet Propulsion Laboratory**
California Institute of Technology
Pasadena, California

www.nasa.gov



**Poster No. P-10**

National Aeronautics and Space Administration

# Chemical Analysis of Lipophilic Biomarkers for Ocean Worlds Using Carbon Dioxide as a Solvent

**Victor Abrahamsson (3227), Bryana Henderson (3227)**
**Fang Zhong (382), Isik Kanik (3220) and Ying Lin (4210)**

## Introduction

Evidence of past or present life, and sustainability of future life, are currently principal topics in space exploration. Chemical analysis of organic molecules that function as biomarkers through in situ robotic missions (to Ocean Worlds such as Europa or Enceladus, for example) will be vital in this effort.

Historically, attempts to detect organics on Mars have been hindered by degradation, reactions and contamination, which highlights the importance of robust and capable sample handling and preparation [1-2].

Supercritical $CO_2$ offers an alternative approach free of organic solvents, buffers and derivatization reagents; and is employed at mild temperatures (40-60 °C) [3-4].

## Goal

Our aim is to develop an end-to-end methodology that enables quantitative analysis of organic biomarkers from Ocean Worlds using only $CO_2$ as a solvent.

The first objective of this work is to develop a methodology which can extract, preconcentrate and separate as wide of a range of nonpolar molecules as possible without degradation. Future work will address the second objective of covering polar molecules.

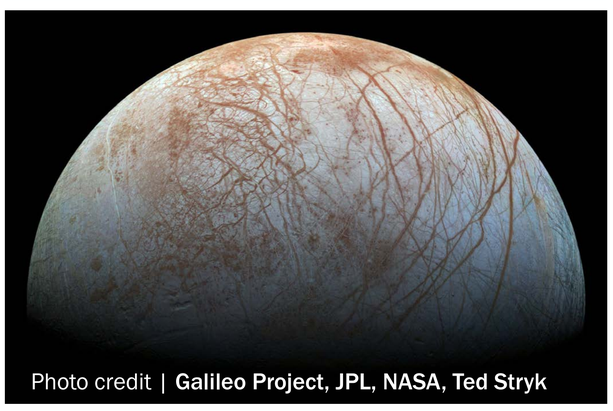


**Fig. 1** Our instrument can be used to extract and analyze organics from mixed ice/regolith/water samples on Ocean Worlds such as Europa.

**National Aeronautics and Space Administration**
**Jet Propulsion Laboratory**
California Institute of Technology
Pasadena, California

www.nasa.gov



## Experimental

**Extraction**
- Solid, aqueous or mixed sample
- $CO_2$ is used as the extraction solvent
- 1-5 g of sample
- Diatomaceous earth (mainly silica) is used for supporting aqueous samples
- Extraction conditions: 22 MPa, 40 °C and 1 g/min of supercritical $CO_2$ for 40 min

**Pre-concentration**
- The extraction solvent ($CO_2$) is depressurized into gas
- The compounds are pre-concentrated on the trap
- The performance of the trap is independent of the sample volume – a larger sample can further improve detection limits

**Separation**
- Chromatography is used to separate the molecules
- Only $CO_2$ is used as a solvent
- Same material is used as in the trap
- Separation facilitates the identification of unknown compounds

**Detection**
- Any chemical detector can be interfaced
- We employed absorption spectroscopy and mass spectrometry
- Electrospray ionization as ionization source before a quadrupole mass spectrometer
- The data output is represented in **Fig. 3**

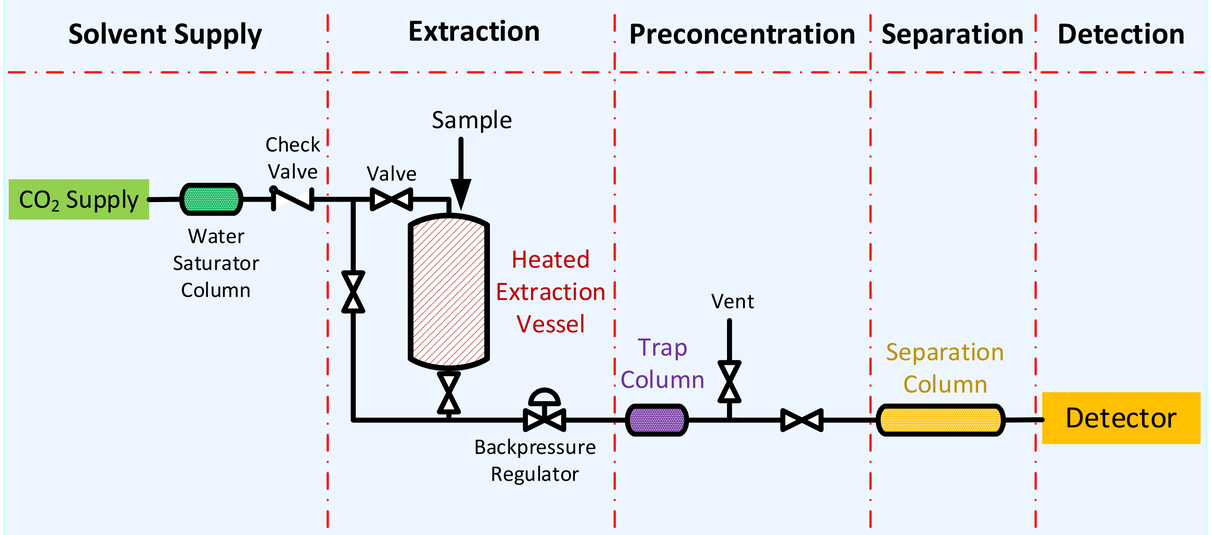


**Fig. 2** Schematic of the instrumentation used for detecting biosignatures from solid, aqueous, or mixed solid/aqueous samples with or without high salt content.

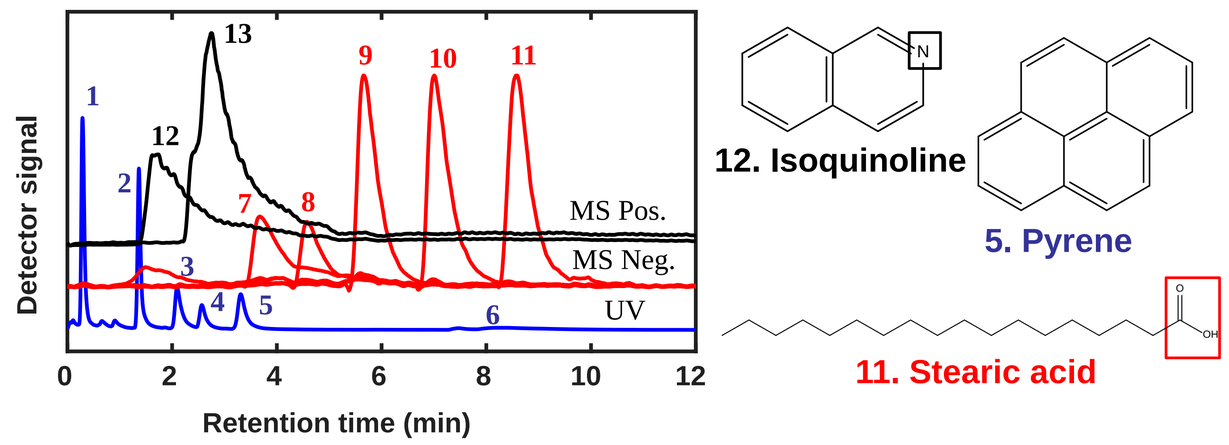


**Fig. 3** The chromatogram represents the condensed data output from the instrumentation. Each peak represents a separated compound. The retention times and the pure spectra of each peak provides information for identification of unknown compounds (also see **Table 1**).

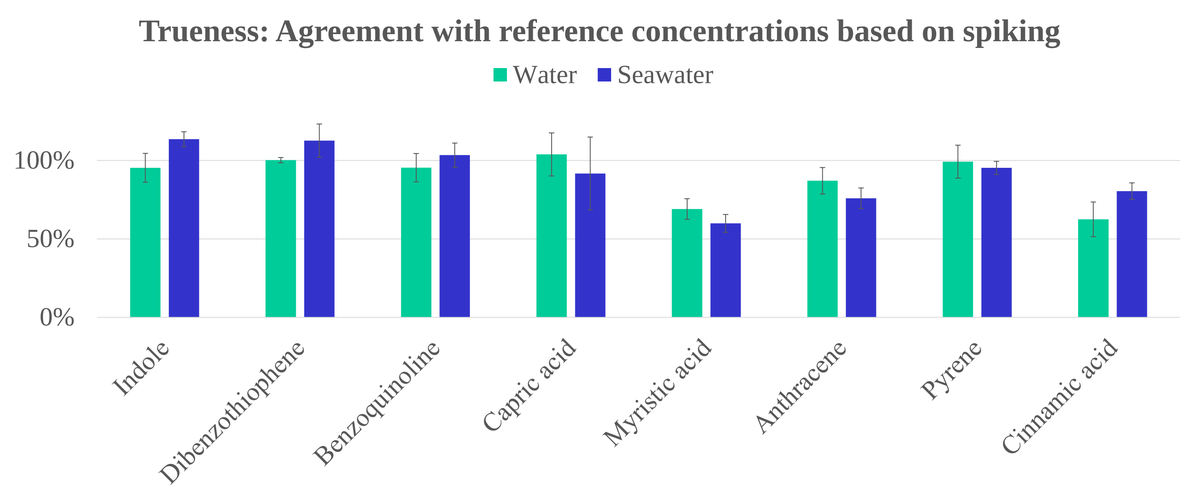


**Fig. 4** The trueness reflects how close the measured concentration of the sample is to the actual value, where 100% is perfect agreement. Water and seawater (3% salt) were both spiked with target compounds. The salt concentration did not interfere with the quantitative analysis.

## Results and discussions

Nonpolar compounds (e.g. bases, acids, oxygen, nitrogen and sulfur-containing compounds with a range of hydrophobicities and volatilities) were successfully extracted, trapped and separated.

The extraction efficiency (recovery) was over 70% for 16 of 18 evaluated biomarkers. The limits of detection (LOD) ranged from low ppb's down to low ppt's (see **Table 1**).

**Table 1.** Compounds shown in the chromatogram and their LODs.

| Peak number | Compound | Detector | LOD |
|---|---|---|---|
| 1 | Napthalene | UV | 1 µg/L |
| 2 | Anthracene | UV | 1 µg/L |
| 3 | 9-Phenylanthracene | UV | 2 µg/L |
| 4 | Fluoranthene | UV | 9 µg/L |
| 5 | Pyrene | UV | 2 µg/L |
| 6 | Cinnamic acid | UV | 10 µg/L |
| 7 | Capric acid | MS (ESI Neg.) | 20 µg/L |
| 8 | Lauric acid | MS (ESI Neg.) | 60 µg/L |
| 9 | Myristic acid | MS (ESI Neg.) | 30 µg/L |
| 10 | Palmitic acid | MS (ESI Neg.) | 20 µg/L |
| 11 | Stearic acid | MS (ESI Neg.) | 30 µg/L |
| 12 | Isoquinoline | MS (ESI Pos.) | 10 ng/L |
| 13 | Acridine | MS (ESI Pos.) | 10 ng/L |

## Conclusions

With our newly developed methodology, we are able to extract, preconcentrate, separate and detect lipophilic compounds, which we demonstrate with an array of polycyclic aromatic hydrocarbons, pigments and free fatty acids. The chemical analysis of biomarkers is possible from either solid or aqueous samples, even with a high salt content, without causing degradation.

## Acknowledgements

This research was enabled through funding from NASA's Concepts for Ocean Life Detection Technology (COLDTech) Program and prior funding from NASA's ASTID program. This research was carried out at the Jet Propulsion Laboratory, California Institute of Technology, under a contract with the National Aeronautics and Space Administration.

## References

**[1]** Stalport, F., et al. (2012). Planet. Space Sci 67: 1-13. **[2]** Leshin, L. A., et al. (2013). Science 341: 1238937. **[3]** McCaig, H. C., et al. (2016). Astrobiology 16: 703-714. **[4]** Menlyadiev, M., et al. (2018). Int. J. Astrobiol: 1-10.

**Poster No. P-11**

National Aeronautics and Space Administration

# Spectroscopy of radicals in outer Solar System ice analogs

**Edith Fayolle (3227)**
Robert Hodyss (3227), Paul Johnson (3220), Xu Zhang (329H), Stanley Sander (3290)
Jet Propulsion Laboratory, Californian Institute of Technology

**The presence of radicals in outer Solar System ices is signpost of the surface weathering history. They should be search for in New Horizons spectra.**

New Horizons spectroscopic instruments are and will provide a wealth of spectral information to characterize the composition of atmospheres and surfaces on outer Solar System bodies. KBOs surfaces are mostly dominated by $N_2$ ices and smaller amounts of $CH_4$ and CO.

Based on laboratory irradiation of ices by photons or energetic particles, radicals like $CH_3$, $CH_3CH_2$, or CN are expected to be trapped in these icy surfaces.
To identify radicals in surface spectra and thus investigate energetic history of the outer Solar system bodies surfaces, radicals electronic and vibrational transitions frozen in $N_2$ ice need to be known.

Previous experiments focused on irradiating ice mixtures with energetic particles to produce radical species but the low productions rate prevent spectroscopic measurements at frequencies relevant to New Horizons instruments (1.25-2.5 µm for LEISA and 52-187 nm for ALICE).

Here, we optimize a radical species production source based on pyrolysis previously employed for atmospheric studies.

*2005 FY9 aka Makemake*
*Credit: NASA/ JPL-Caltech*

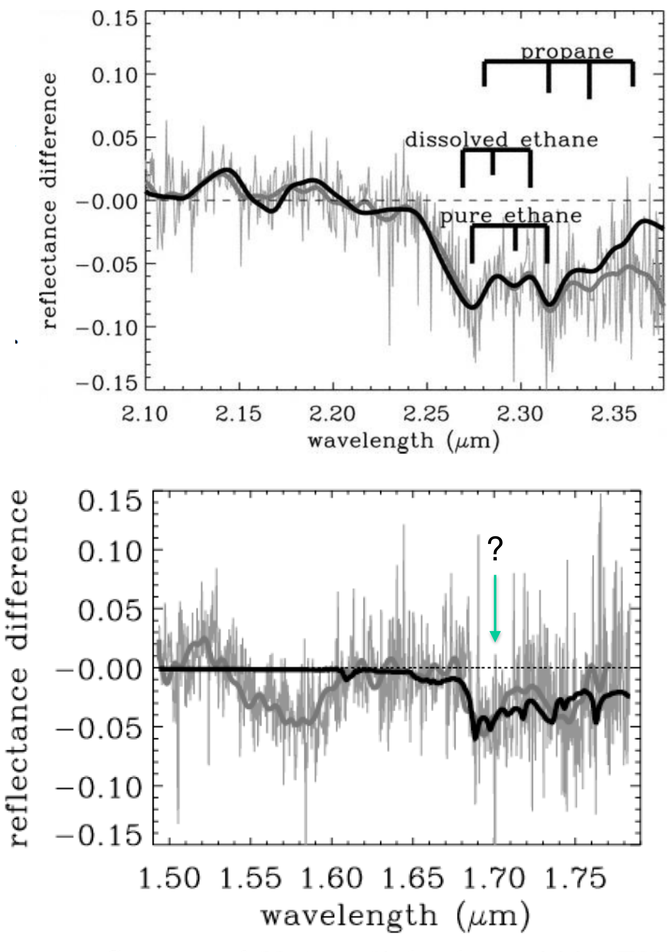


*Spectra of Kuiper Belt object 2005 FY9*
*Brown et al 2007*

**Determining radical spectroscopic transitions in the New Horizons accessible frequency range is not trivial**

Ab-initio calculations based on the radical species geometry can be undertaken to estimate and yield good results for gas phase spectroscopic assignments. In an ice matrix, however, such as the ones encountered on cold icy bodies dominated by $N_2$, frequency shifts occur depending on the concentration and configuration of the radical in its molecular environment.

Experiments are necessary to build spectroscopic database and allow a reliable interpretation of spectroscopic observations.

*CH-stretch vibration frequency for the methyl radical in different environments (NIST database)*

| Frequency ($cm^{-1}$) | Environment |
|---|---|
| 3160.821 | Gas |
| 3162 | Ne |
| 3150 | Ar |
| 3171 | $H_2$ |

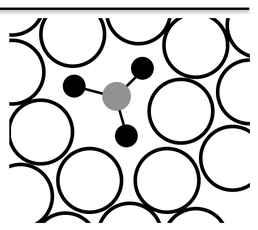

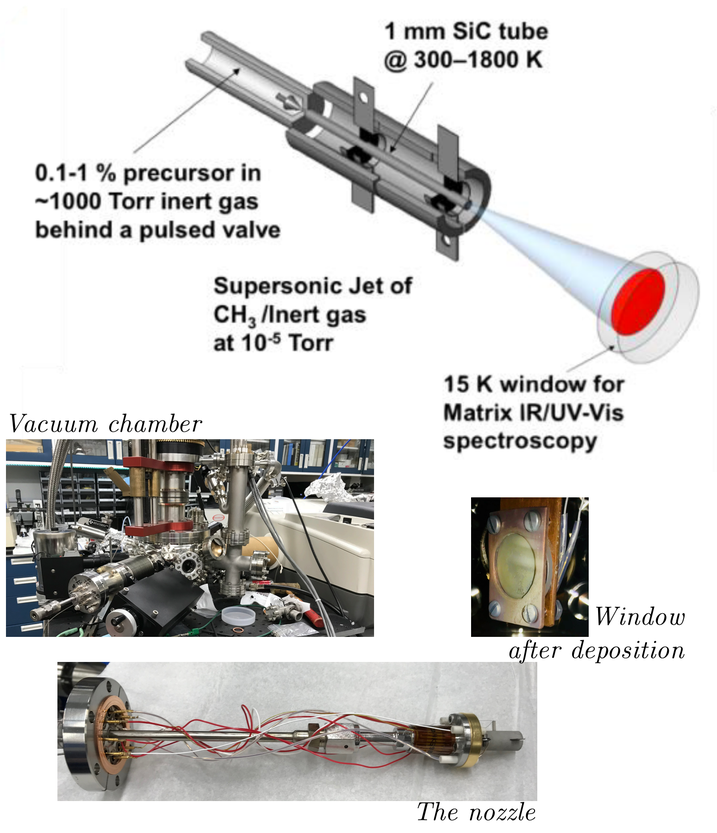


### *Laboratory setup*

Radicals are produced in a supersonic pyrolysis nozzle by thermally cracking specific reactants in $N_2$.

The radical-$N_2$ beam is expanded into a vacuum chamber and condensed onto a cryogenically-cooled window.

*Vacuum chamber*





*Window after deposition*



*The nozzle*

The isolation of radicals by the matrix allows to perform spectroscopic measurements and derive frequencies and band strengths.

Strategy for our project: the fundamental transitions of the radicals are in the mid-IR range and will be searched for first. Operational conditions will be optimized before extended investigation to the near-IR and VUV where transitions are weaker.

**So far:**

- We are still searching for the best conditions to form the methyl radical using the pyrolysis nozzle: temperature, mixture composition, and flow rate.
- Alternative photochemical methods to produce radicals using spectrally characterized bright VUV lamps are being considered.
- It takes more than three months to reproduce in the laboratory what took millions years to form in space.

**National Aeronautics and Space Administration**
**Jet Propulsion Laboratory**
California Institute of Technology
Pasadena, California

www.nasa.gov



Brown, M. E., E. L. Schaller and G. A. Blake (2015) Irradiation Products On Dwarf Planet Makemake The Astronomical Journal 149(3): 105
Hodyss, R., H. R. Howard, P. V. Johnson, J. D. Goguen and I. Kanik (2011) Formation of radical species in photolyzed CH4:N2 ices Icarus 214(2): 748-753.
Zhang, X., A. V. Friderichsen, S. Nandi, G. B. Ellison, D. E. David, J. T. McKinnon, T. G. Lindeman, D. C. Dayton and M. R. Nimlos (2003) Intense, hyperthermal source of organic radicals for matrix-isolation spectroscopy Rev Sci Instrum 74(6): 3077-3086.

**Poster No. P-12**

National Aeronautics and Space Administration

# Laboratory Simulations of Photochemistry in Hot Exoplanet Atmospheres


**Benjamin Fleury (3227)**

**Murthy Gudipati (3227), Bryana Henderson (3227)**


## Introduction

- With new missions such as TESS and JWST on the horizon, challenges are mounting to determine the contributions of aerosols to chemical and radiative coupling in exoatmospheres.
- Photochemistry has the potential to substantially impact the atmospheric composition of exoplanets and lead to the formation of photochemical hazes with consequence on the radiative transfer, thermal structure and dynamics of the atmosphere, particularly in UV-rich stellar environments
- The aim of our work is to undertake laboratory simulations to help determine the equilibrium chemical compositions and aerosols formation efficiencies of exoplanets whose observable atmospheric temperatures vary between 300 K and 1800 K, a range that covers relatively cool terrestrial exoplanets to hot-Jupiter-like-exoplanets.
- Here, we present the results of a first laboratory experimental simulation of photochemistry in carbon-rich (C/O ratio ≥ 1) exoplanet atmospheres at elevated temperatures (Fleury et al. 2018).

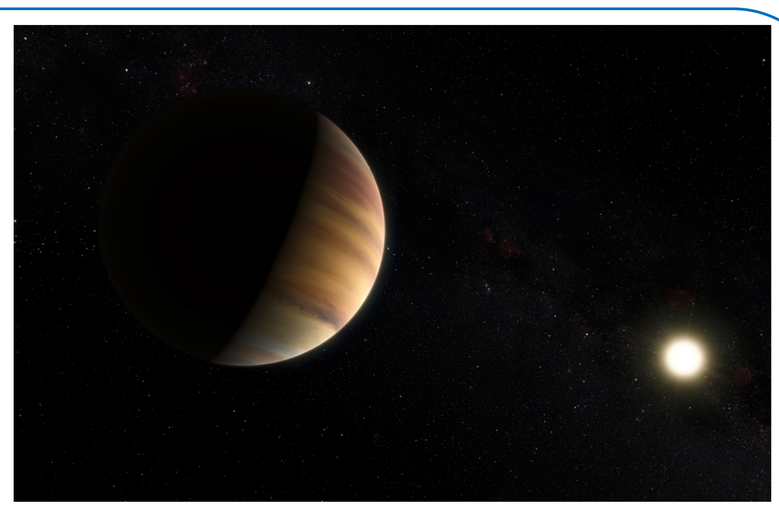

Artistic view of 51 Pegasi B, a Hot-Jupiter like exoplanet. These exoplanet atmospheres experience high temperature and high UV radiation conditions. **Credit:** ESO/M. Kornmesser/Nick Risinger (skysurvey.org)

## Experimental methodology

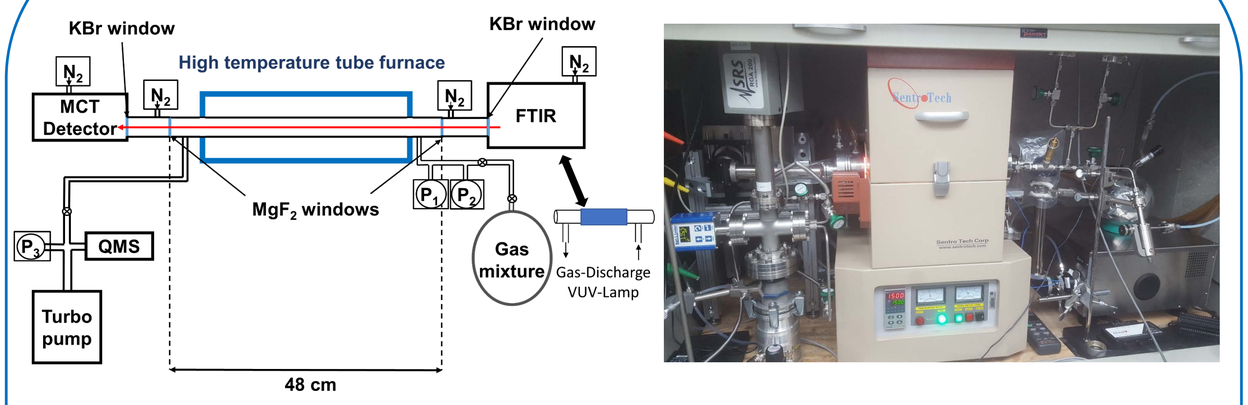


**Figure 1:** *Scheme of the ExoFurnace CAAPSE experiment concept (left) and picture of the CAAPSE in action at 1773 K at JPL (right).*

- We used the CAAPSE experiment ("Cell for Atmospheric and Aerosol Photochemistry Simulations of Exoplanets"), recently built at JPL (Figure 1).
- The cell was filled with 15 mbar of $H_2$:$^{13}CO$ mixture with a mixing ratio of 99.7%:0.3% and then warmed up to the studied temperatures.
- Then the heated gaseous mixture was irradiated in the UV (Ly-α, 121.6 nm) using a microwave discharge lamp flow with $H_2$.
- Gas phase composition was monitored using IR spectroscopy and mass spectrometry.

## Thermal Equilibrium Composition vs. Photochemistry

The room-temperature spectrum contains the absorption band of the initial $^{13}CO$ (2095 $cm^{-1}$).

The spectra of the heated gases also reveal the formation of bands due to two new (thermally-generated) molecular species: $^{13}CO_2$ (2284 $cm^{-1}$) and $^{13}CH_4$ (3009 $cm^{-1}$). These two new species are isotopically labelled with $^{13}C$, highlighting that they are formed during thermal chemistry from the initial $^{13}CO$.

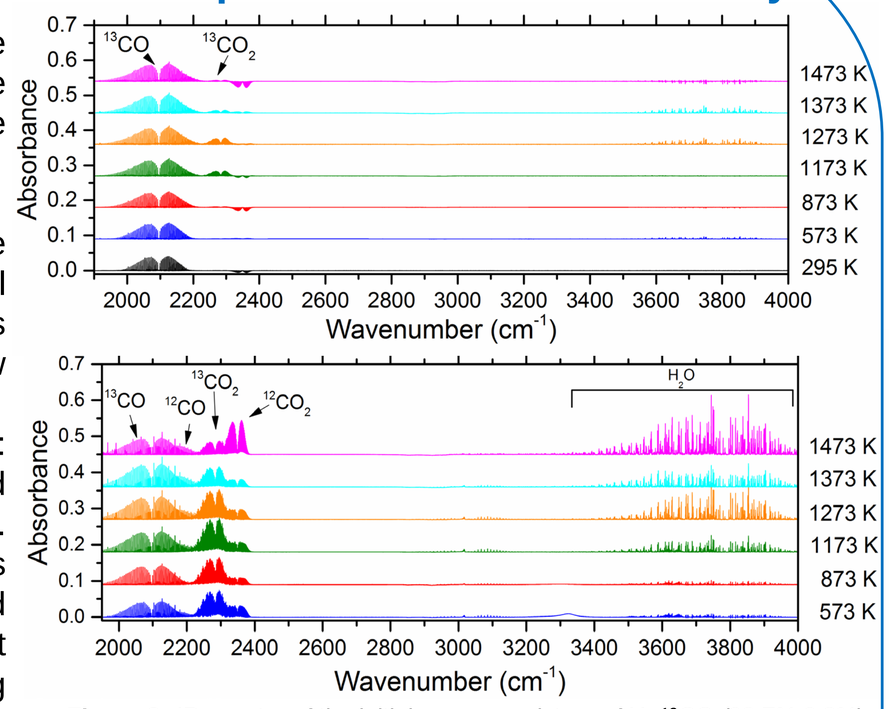


**Figure 2:** *IR spectra of the initial gaseous mixture of $H_2$:$^{13}CO$ (99.7%:0.3%) at 295 K and at the equilibrium for different set oven temperatures: 573 K, 873 K, 1173 K, 1273 K, 1373 K, and 1473 K (top) and after 18 hours of irradiations at 121.6 nm (Ly-α) (bottom); spectra are offset for clarity,*

UV (121,6 nm, Ly-α) irradiation of the heated gases leads to a decrease of [CO], an increase of [$CO_2$], and the formation of water.
Photochemistry can strongly influence the composition of $H_2$:CO warm exoplanet atmospheres. $CO_2$ and $H_2O$ can be efficiently produced in these atmospheres despite competitive loss processes. The gas temperature strongly influences the efficiency of the different chemical pathways, notably due to the increase of the absorption cross-sections of $CO_2$ when the temperature increases.

## Organic aerosols formation

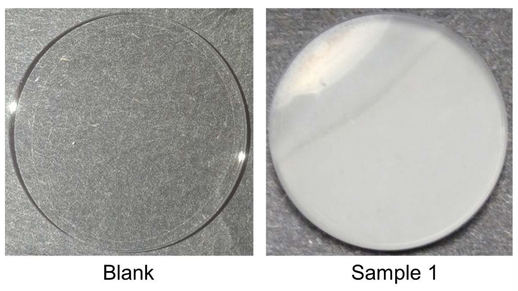


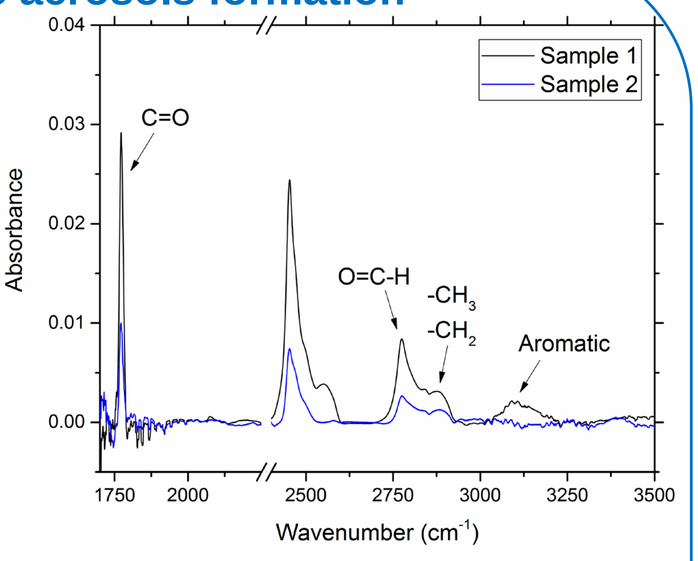


**Figure 3:** Left: *photographs of a blank sapphire window and an organic film deposited on sapphire windows during the experiments realized with $H_2$:CO (300:1) gas mixture at 1473 K with UV-irradiation (Ly-α).* Right: *IR absorption spectra of the organic aerosols.*

- We have observed the formation of solid organic thin films after the irradiation of the gas phase at 1473 K with Ly-α.
- We found that non-volatile hydrocarbon aerosols are formed with HCO-functionality involving aromatic and aliphatic hydrocarbons.
- This result demonstrates that refractory organic aerosols can be efficiently formed in hot exoplanet atmospheres with an enhanced C/O ratio.

## Conclusions

- We found that $H_2$/CO gas compositions can differ significantly from thermal equilibria compositions at temperatures ranging from 600 K to 1500 K when irradiated with Ly-α photons.
- Carbon dioxide and water were found to be the main products, while formation of methane was also observed to a lesser extent. We find that photochemistry efficiency is strongly correlated with increasing temperature. Our finding that water is efficiently produced by photochemistry in a super Solar C/O=1 environment has significant implications for the interpretation of many exoplanet transmission spectra.
- We also find the formation of an organic solid condensate at 1500 K and under Ly-α UV-radiation, confirming the possibility of forming photochemical hazed in hot-Jupiter exoplanet atmospheres with an enhanced C/O ratio compared to Solar.


**National Aeronautics and Space Administration**

**Jet Propulsion Laboratory**
California Institute of Technology
Pasadena, California

www.nasa.gov





### Acknowledgments

This research work has been supported by the Strategic R&TD funding under "Exoplanet Science Initiative, ESI". We thank Dr. Mark Swain for helpful discussions.


### References


**B. Fleury**, M. Gudipati, B. Henderson, M. Swain, *Photochemistry in hot $H_2$-dominated exoplanet atmospheres*, submitted to ApJ.


**Poster No. P-13**

National Aeronautics and Space Administration

# Chemical Evolution of Complex Organics in Ices

## From Interstellar Ice to Comets

**Daniel Paardekooper (3227), Bryana Henderson (3227) and Murthy Gudipati (3227)**

***Abstract**:* In various environments, many Complex Organic Molecules (COMs) have been detected, however the conditions under which they are synthesized are still unconstrained, leaving a large gap in our knowledge. The fundamental laboratory study described here will address this missing link using cutting edge techniques; novel for this field of science.

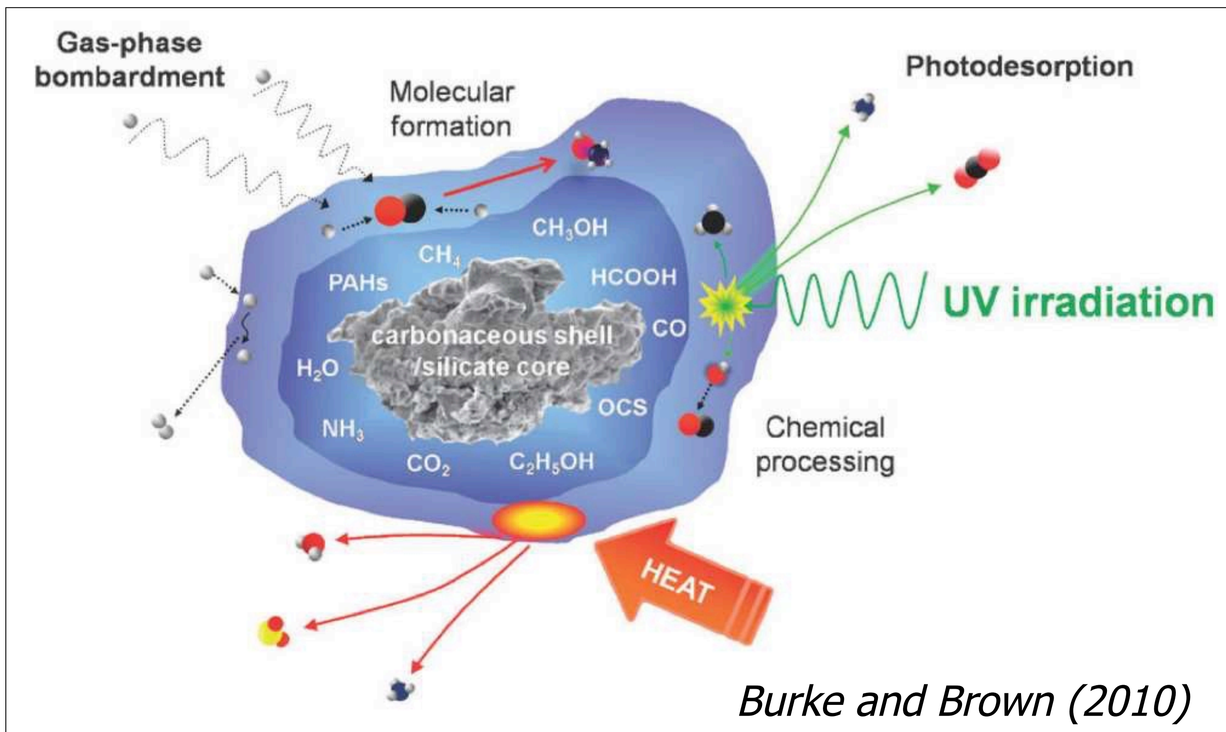


*Burke and Brown (2010)*

***Introduction**:* Dust grains play an essential role in the evolution of Complex Organic Molecules (COMs). They provide a meeting place for atoms and molecules to accrete and find reaction partners. Such grains are covered with ice, consisting of simple volatile molecules such as $NH_3$, CO, $CH_3OH$ and $H_2O$.

***Approach**:* IR laser ablation (2948 nm) of energetically processed interstellar ice analogues, in conjunction with a Quadrupole Mass Filter allows isolation of ions of interest for further analysis.

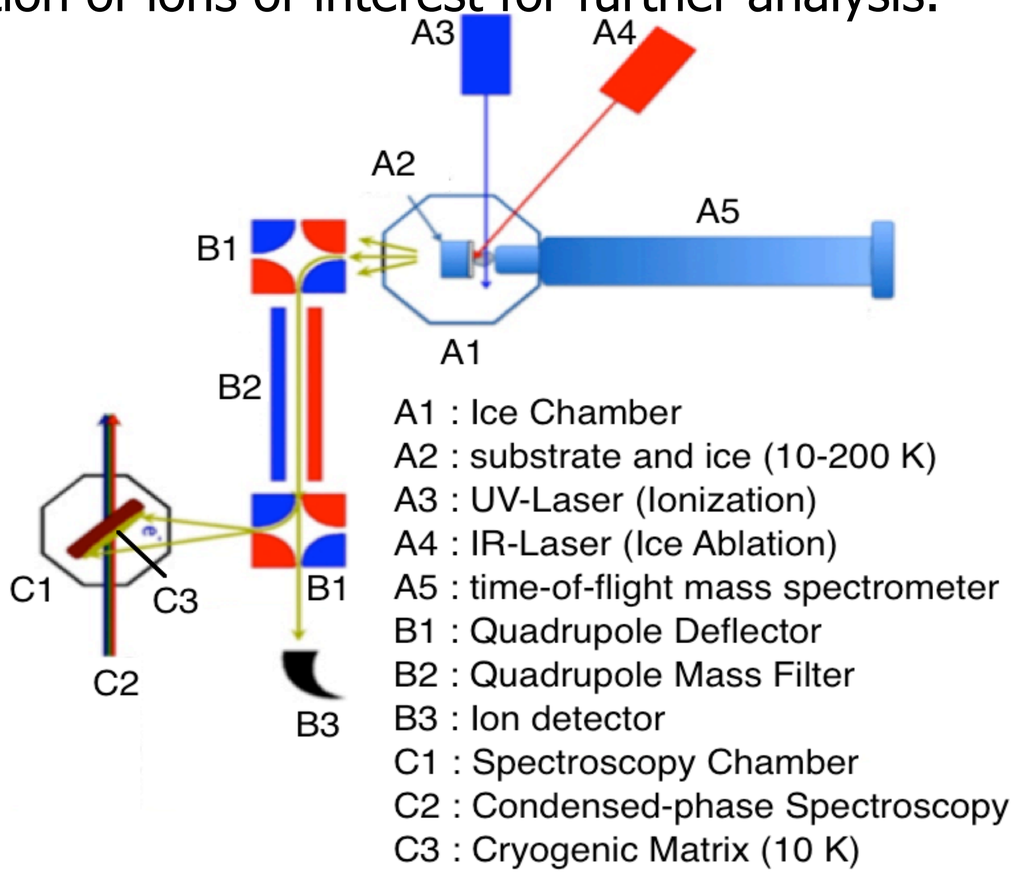


*The **ultimate goal** is to understand when and where complex organics including prebiotic molecules are formed in space – from interstellar ice grains through protoplanetary disks to cometary precursors such as KBOs (Kuiper Belt Objects).*

Comets are understood to be a direct link to interstellar ice grains, capable of bringing prebiotic COMs to Earth during the formation of our Solar system, providing the ingredients and perhaps even **triggering** the origin of life on Earth.

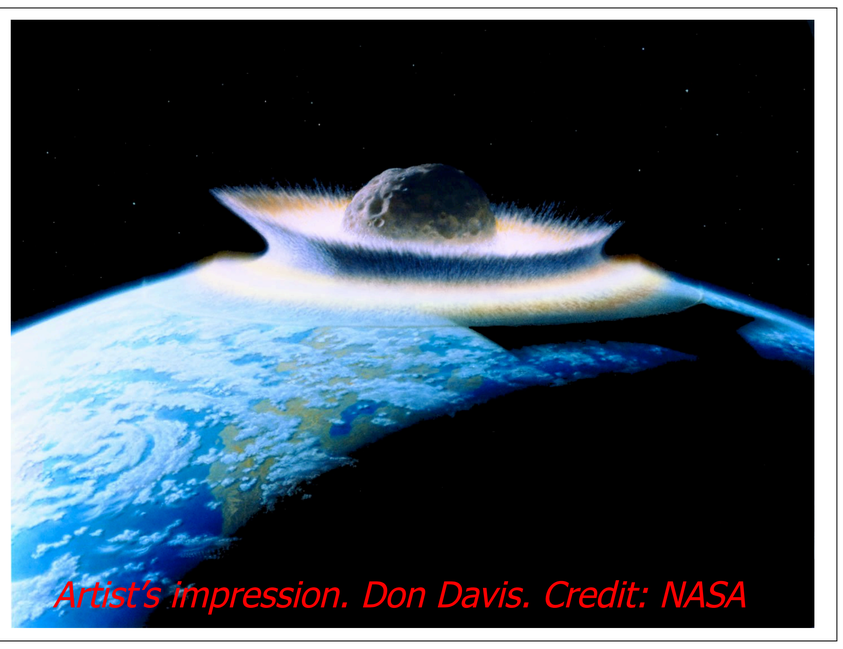

*Artist's impression. Don Davis. Credit: NASA*

Research described here is timely, since it provides guiding for past, current and future facilities/missions:

- *Atacama Large Millimeter Array* (ALMA) if fully operational.
- Rosetta mission (ESA) has recently ended and provided unique information.
- James Web Telescope (JWST) will be launched in 2020.

**National Aeronautics and Space Administration**
**Jet Propulsion Laboratory**
California Institute of Technology
Pasadena, California

www.nasa.gov



***References:*** M.S. Gudipati and R. Yang. *Astrophysical Journal Letters 746 (2012) L24*
D.M. Paardekooper, J.-B. Bossa, K. Isokoski and H. Linnartz. Review of Scientific Instruments, 85, (2014) 104501
B.L. Henderson and M.S. Gudipati. *Astrophysical Journal 800 (2015) 66*
D.M. Paardekooper, J.-B. Bossa and H. Linnartz. *Astronomy & Astrophysics, 592, (2016) A67*

***Acknowledgements**: This work has been carried out at Jet Propulsion Laboratory, California Institute of Technology under a contract with the National Aeronautics and Space Administration, and funded by JPL's R&TD Program and NASA Solar System Workings Program. DMP thanks NASA Postdoctoral Program (NPP) Fellowship.*

**Poster No. P-14**

National Aeronautics and Space Administration

# Characterization of microbial communities in harsh environments and their impact on future space missions

**Camilla Urbaniak (352N)**
Ryan Hendrickson (352N), Kasthuri Venkateswaran (352N)

## Background

The **Jet Propulsion Laboratory** has been building spacecraft for decades, sending missions into outer space, to explore our solar system and beyond.

As exciting as it is to create these rovers, landers and satellites that probe the vastness of space and stir our imaginations, the trillions of microbes (**bacteria/fungi/viruses**) that surround us are just as important to study as the designs used to create these spacecrafts.

**Microbial monitoring** and control is an essential part of any space mission as these tiny organisms could stow away from Earth, leading to possible contamination of other planets and moons. They could also theoretically induce biocorrosion of spacecraft, leading to material failure and loss of stability.

Here we show the **hardy organisms** that have been **detected in ultra clean and harsh facilities** such as JPL's **spacecraft assembly facility** and the extreme environment of space (**International Space Station**) using state of the art molecular techniques and compared with traditional NASA standard methods.

## JPL SAF Microbiome

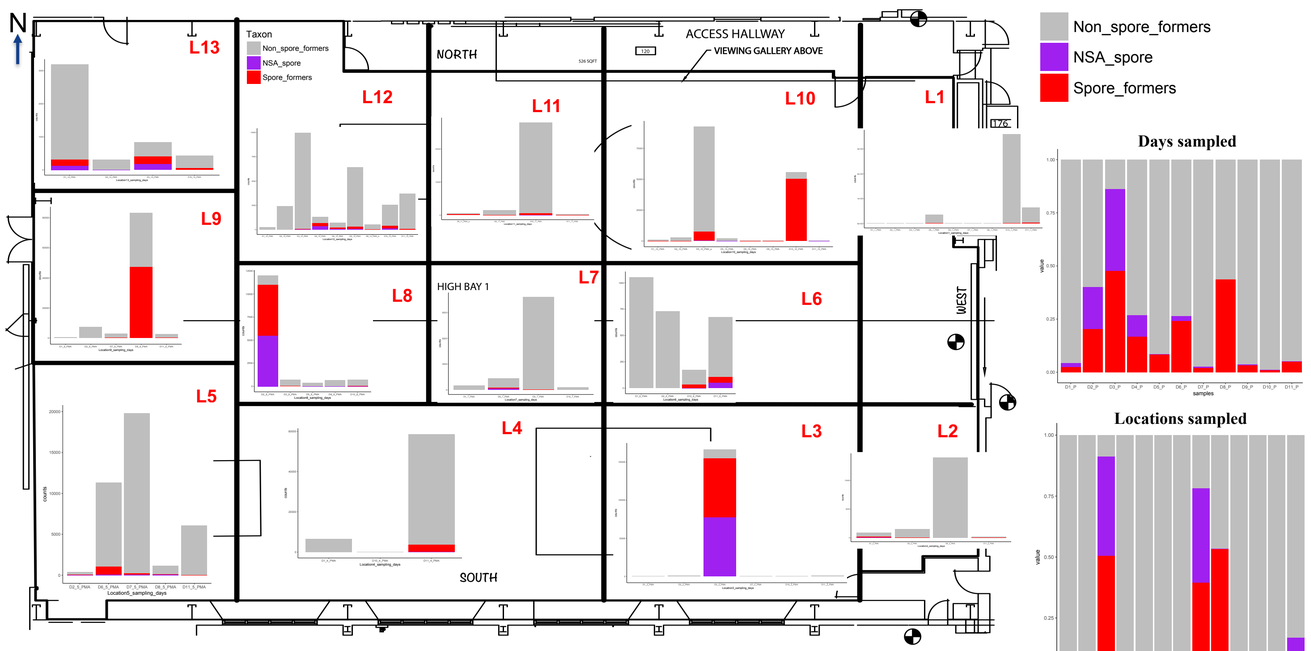


**Figure 1**: **Floor plan of SAF showing proportion of bacteria detected**
DNA sequencing was used to detect viable bacteria from 13 different floor locations across the SAF over a span of 11 days. The proportion of (i) non spore formers (gray), (ii) spores detected with the NASA standard assay (NSA) (purple) and (iii) spore formers not detected by NSA, are shown with the bargraph inside the floor plan. Each bar represents a day sampled and "L" stands for location, with the number representing one of the thirteen locations. The bargraphs to the right of the floorplan summarize this distribution across days sampled (top) and across locations sampled (bottom).

| NSA© spores | Spore formers not detected by NSA© | |
|---|---|---|
| Actinomyces | Alicyclobacillus | Dorea |
| Bacillus | Anoxybacillus__kestanbolensis | Epulopiscium |
| Bacillus_cereus | Brochothrix | Exiguobacterium |
| Bacillus_clausii | Candidatus Arthromitus | Geobacillus |
| Bacillus_coagulans | Clostridiaceae | Geobacillus_thermodenitrificans |
| Bacillus_firmus | Clostridiaceae_SMB53 | Paenibacillaceae |
| Bacillus_flexus | Clostridium | Paenisporosarcina |
| Bacillus_foraminis | Clostridium_bifermentans | Planifilum |
| Bacillus_muralis | Clostridium_bowmanii | Thermoactinomyces |
| Brevibacillus | Clostridium_colinum | Thermoanaerobacterium_saccharolyticum |
| Paenibacillus | Clostridium_hiranonis | Ureibacillus |
| Virgibacillus | Clostridium_perfringens | |
| | Clostridium_saccharogumia | |

**Table 1**: **List of spore formers detected in the SAF by DNA sequencing**
Bacteria detected with DNA sequencing consist of those those detected with the NSA© (heat shock, followed by plating) and spore formers that were not detected with the NSA©

## International Space Station Microbiome

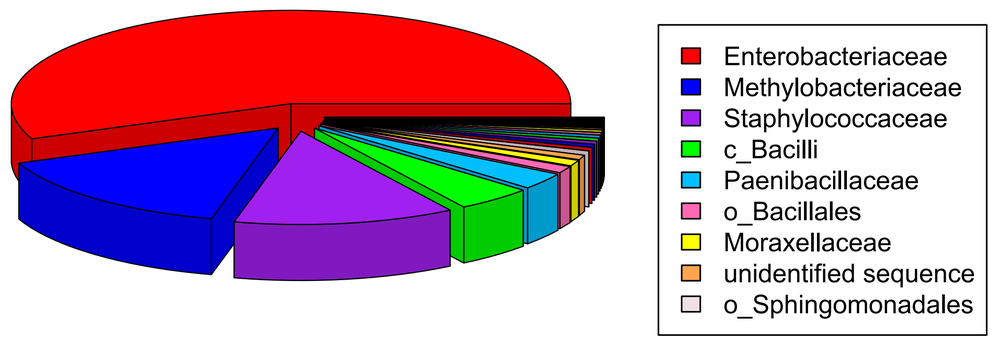


**Figure 2**: **Pie chart showing the relative abundances of bacteria detected on the ISS**
DNA sequencing was used to detect viable bacteria from 8 locations across the ISS, sampled 3 times over a span of 14 months. Combining all samples collected, the highest proportion of bacteria were *Enterobacteriaceae*, a human associated microbe and *Methylobacteriaceae*, an environmental microbe.

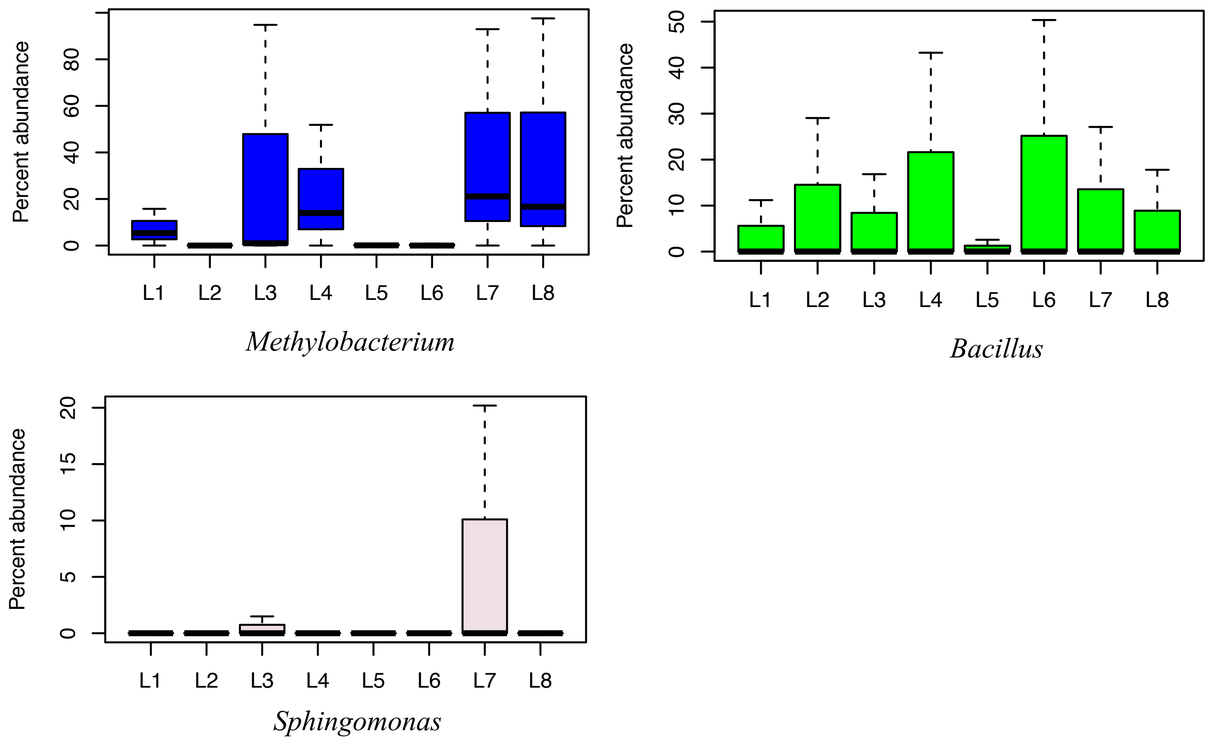


**Figure 3**: **Spatial distribution of bacteria implicated in biocorrosion**
Three different bacteria, documented to be responsible for microbially induced corrosion on Earth, were detected in high numbers on the ISS. The boxplots show the proportion of each bacterium at each location sampled on the ISS. **NB**: High levels of the fungi *Penicillium* and *Aspergillus*, which are also known to induce biocorrosion, were also found in high levels on the ISS.

## Summary

- Despite the harsh conditions of SAF, viable non spore formers exist
- There are spores that are present in SAF that were detected with molecular techniques and failed to get detected by NSA©
- The ISS contains diverse microbial communities with high levels of bacteria and fungi that could cause biocorrosion
- JPL cleanrooms, ISS surfaces/air and Mars-like human occupied habitats all differ in the type and amount of bacteria that survive there

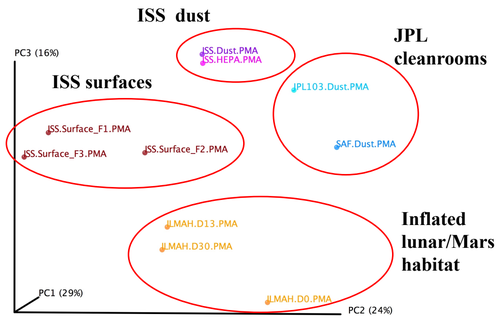


**Figure 4**: **Microbiome comparison**
Different harsh environments were compared to examine the viable bacteria that survive in these locations. JPL cleanrooms have different bacteria than the ISS, which differs from Mars-like human occupied habitats.

**National Aeronautics and Space Administration**
**Jet Propulsion Laboratory**
California Institute of Technology
Pasadena, California
www.nasa.gov


**Poster No. P-15**

National Aeronautics and Space Administration

# Power Laws of Gravity and Topography for Solar System Bodies


**Anton I. Ermakov (392R)**
**Ryan S. Park (392R), Bruce G. Bills (3224)**


## 1. Introduction

- The RMS power spectrum of the gravity field typically follows a power law, also known as the Kaula rule [1].
- A similar rule (a.k.a Vening Meinesz rule) can be derived for a topography power spectrum [2].

**Q: What does the RMS power spectrum tell us?**
**A: It tells us how tall or deep the "mountains" and "valleys" are depending on their horizontal extent**

**Q: Why we need to know topography power spectrum?**
**A: We can estimate the gravity power spectrum from the topography power spectrum.** + do science

**Q: Why we need to know gravity power spectrum?**
**A: We need to know the gravity power spectrum to predict the amplitude of perturbations acting on the spacecraft.** + do more science

**Q: Can we figure out the gravity power spectrum from theory or we fit an empirical spectrum to the observations?**
**A: Actually, we do both and this is what this poster is about.**

## 2. Theory

Shape and gravity in spherical harmonics

$$r(\phi,\lambda) = R\sum_{n=0}^{\infty}\sum_{m=-n}^{n} h_{nm}Y_{nm}(\phi,\lambda) \qquad U(\mathbf{r}) = \frac{GM}{r}\sum_{n=0}^{\infty}\sum_{m=-n}^{n}\left(\frac{R_0}{r}\right)^n g_{nm}Y_{nm}(\phi,\lambda)$$

$R$: mean radius; $R_0$: reference radius; $g_{nm}$, $h_{nm}$: spherical harmonic of degree $n$ and order $m$; $\lambda \approx 2\pi/n$: wavelength

**RMS spectra →**

$$M_n^{gg} = \sqrt{\frac{\sum_{m=-n}^{n} g_{nm}^2}{2n+1}} \qquad M_n^{tt} = \sqrt{\frac{\sum_{m=-n}^{n} h_{nm}^2}{2n+1}}$$

**Assumption made by Kaula:** Topography $h$ is limited by constant strength

**Stress perturbation** $\Delta\sigma = \rho_c g h$ ($\rho_c$: crustal density; $g$: gravit)

$$h = \frac{\Delta\sigma_{\max}}{\rho_c g}$$

Assuming: $\rho_c = \bar{\rho} \equiv \rho$

$h \propto R \cdot M^{tt}$ **therefore:** $M^{tt} \propto \rho_c^{-1} g^{-1} R^{-1} \propto \rho_c^{-1}\bar{\rho}^{-1} R^{-2} \rightarrow M^{tt} \propto g^{-2}$ ($\bar{\rho}$: mean density)

**Gravity from shape →** $g_{nm} \approx \frac{3}{2n+1}\cdot\frac{\rho_c}{\bar{\rho}}\cdot h_{nm} + higher\ order\ terms \rightarrow M^{gg} \propto g^{-2}$

**In summary: gravity and topography power spectra should scale as $g^{-2}$**
**Is it really so? See next sections.**

## 3. Data

- We have used shape and gravity models for terrestrial planets, the Earth's Moon, icy satellites and minor bodies.
- The topography spectra of the icy bodies display the most variability and are not typically determined to a high degree. Therefore, icy bodies' spectra were excluded from further analysis.
- The filled circles represent the portions of the spectra that are linear in a log-log plot and, therefore, correspond to a certain power law. These parts of the spectra were used in fits (Section 4)

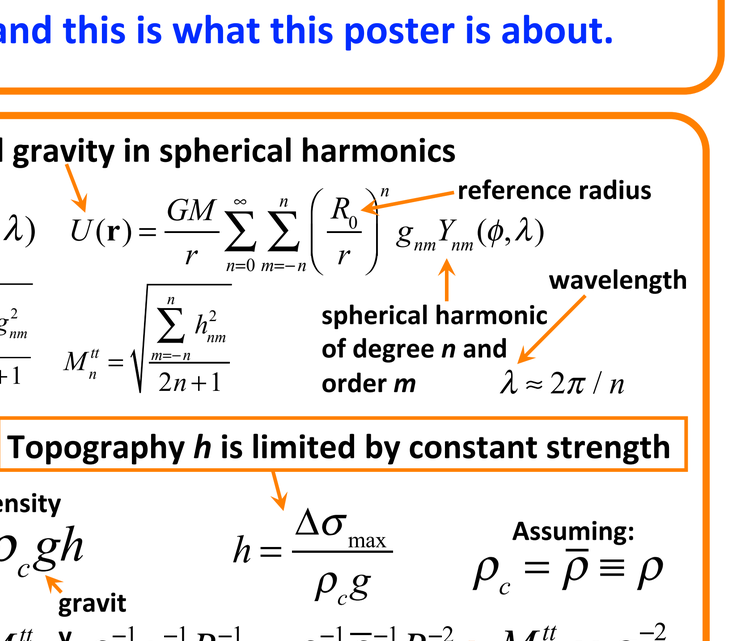


- Topography data sources

Moon, Mars, Venus: Wieczorek, 2015; Mercury: Becker et al., 2016; Earth: Hirt & Kuhn, 2012; Phoebe, Mimas, Tethys, Dione: Gaskell, 2013; Itokawa: Gaskell, 2008; Toutatis: Hudson et al., 2008; Eros: Zuber et al., 2000; Vesta: Gaskell, 2012; Phobos: Gaskell, 2011.

- Gravity data sources

Earth: Pavlis et al., 2008; Mars: Konopliv et al., 2016; Mercury et al., 2014; Moon: Konopliv et al., 2013; Venus: Konopliv et al., 1999; Vesta: Konopliv et al., 2014.

## 4a. Results for topography

- We used Markov chain Monte-Carlo method implemented in `emcee` library [3] to fit the general topography power laws of planets and asteroids

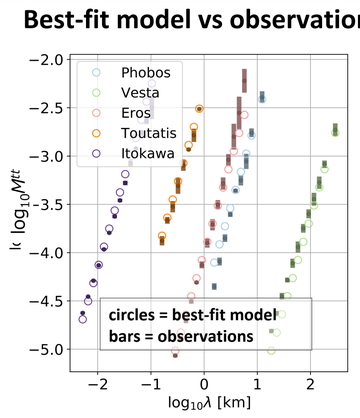


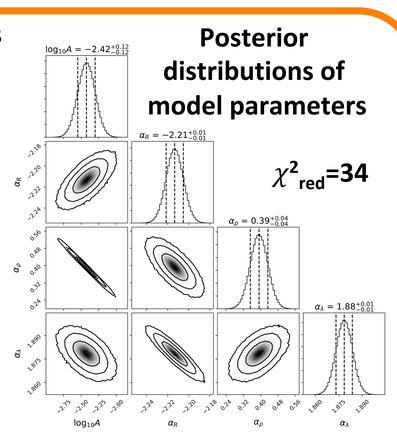


- We try a more general model with four parameters:

$$M^{tt} = AR^{\alpha_R}\rho^{\alpha_\rho}\lambda^{\alpha_\lambda}$$

since $g \propto R\rho$
expect $M^{tt} = AR^{-2}\rho^{-2}\lambda^{\alpha_\lambda}$
Our results *somewhat* agree with the expectation

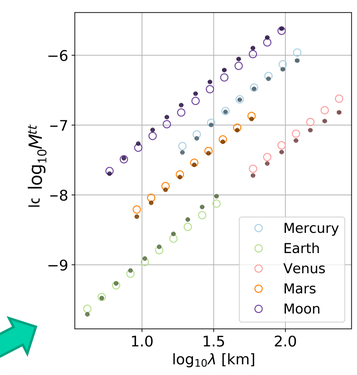


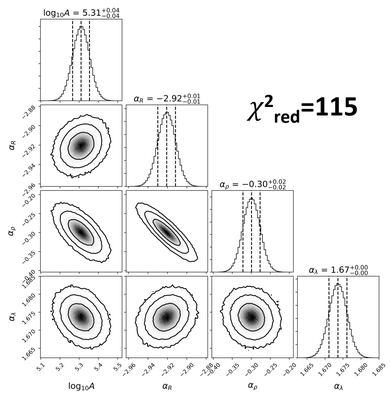


## 4b. Results for gravity

- The selection of the bodies with known gravity is smaller
- Therefore, we choose only three-parameter model:

$$M^{gg} = Bg^{\beta_g}n^{\beta_n}$$

General agreement with expectation

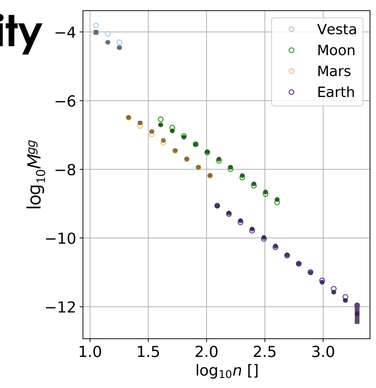


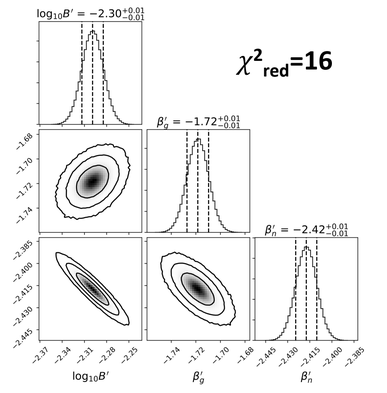


## 4c. Prediction for Psyche

- We have used the observed mean radius and density of Psyche to estimate its gravity RMS spectrum using the scaling derived in 4a.
- We generated an ensemble of pseudorandom shape from which we computed gravity.
- The ranges of the gravity RMS spectrum will be useful for the Psyche radio-science planning

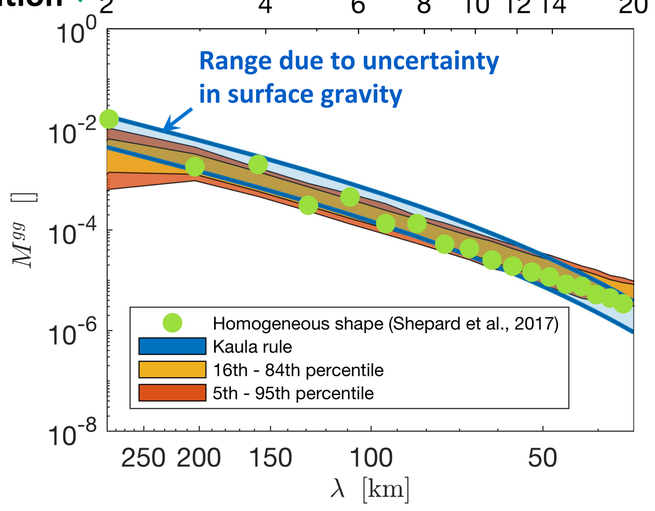


- Kaula-rescaled Earth gravity RMS agrees surprisingly well with psudorandom gravity-from-shape of Psyche.

## 5. Conclusions

- We have analyzed topography and gravity RMS spectra of the bodies that have gravity and shape models sufficiently accurate for spectral analysis.
- We have found that despite having different internal structure, composition and mechanical properties, the topography RMS spectrum of minor bodies can be effectively modeled with a general power law that depends on the radius and the mean density of the body.
- For the case of the terrestrial planets, there are significant systematic discrepancies between the maximum likelihood general scaling model fit and the observed RMS spectra.
- A procedure was proposed to provide an a priori constraint on the RMS gravity spectrum for minor bodies.

## 6. References:


[1] W.M. Kaula. Determination of the Earth's gravitational field. Reviews of Geophysics, 1(4): 507–551, 1963; [2] F.A. Vening Meinesz. A remarkable feature of the Earth's topography. In Proc. K. Ned. Akad. Wet. Ser. B Phys. Sci, volume 54, 1951; [3] D. Foreman-Mackey, D.W. Hogg, D. Lang, and J. Goodman. emcee: the MCMC hammer. Publications of the Astronomical Society of the Pacific, 125(925):306–312, 2013.




**Poster No. P-16**

# Spectral Properties of Fe(III)/Fe(II), Mg, Al Smectites to Improve Planetary Remote Sensing

**Valerie Fox (Caltech, vfox@caltech.edu)**
**Bethany Ehlmann(3320, Caltech), Luther Beegle (3320)**
**Collaborators: Jeffery Catalano, Robert Kupper, Ryan Nickerson (Washington University in St Louis)**

National Aeronautics and Space Administration

- Smectite clays are among the most common aqueous alteration products observed on planetary surfaces.
- Smectite compositions depend on the geochemical and redox environment in which they form.
- To date, well-classified smectite standards are predominately high in Fe(III) and Al (nontronites, montmorillonites, beidellites).

- **Detailed characterization of intermediate composition smectites of different oxidation states are needed to better interpret remote sensing observations and understand aqueous systems throughout the solar system.**

- We have synthesized a suite of 16 intermediate composition smectite samples for detailed spectroscopic analysis, using a hydrothermal sol-gel method (Chemtob+,2015) . Each sample is confirmed to be pure smectite using XRD, and composition is measured using ICP-OES.

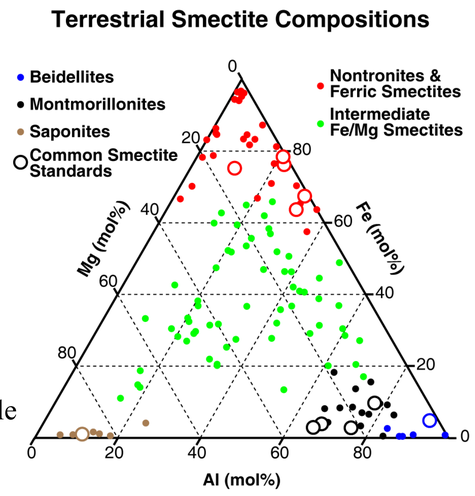


Cation substitution of Al, Fe(III), Fe(II), and Mg into the octahedral layer and Si, Al, and Fe(III) into the tetrahedral layer changes the bond energies as the mineral structure shifts to accommodate charge.
The mineral structure changes from dioctahedral to trioctahedral as more 2+ cations occupy octahedral sites.
In smectites, the interlayer is expandable and can host a variety of molecules.

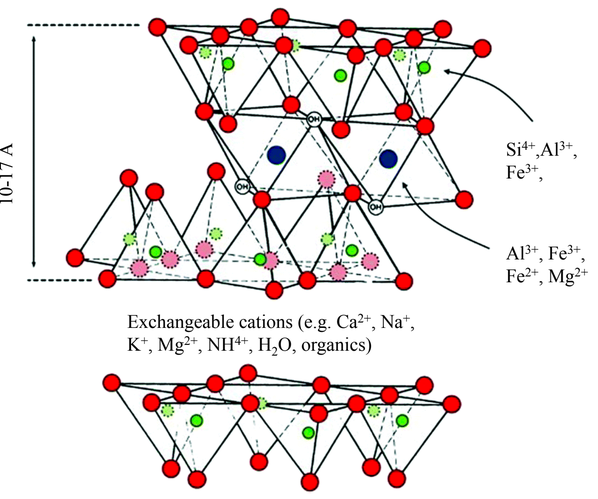


## Ferric Smectites

Octahedral layer composition of ferric smectite samples.

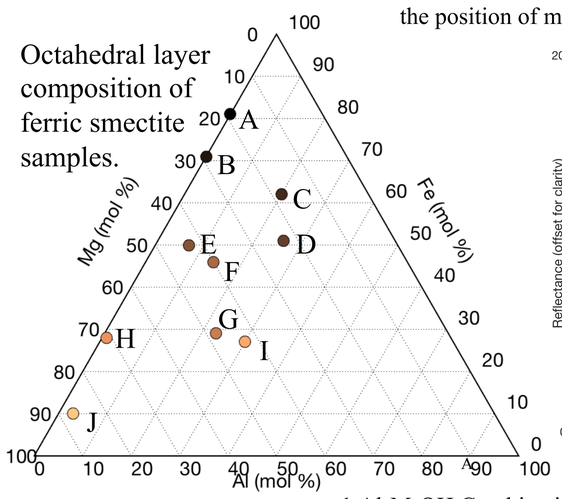


Visible to near infrared reflectance of ferric samples. Composition alters the position of metal-OH combination bands between 2.1-2.5 µm.

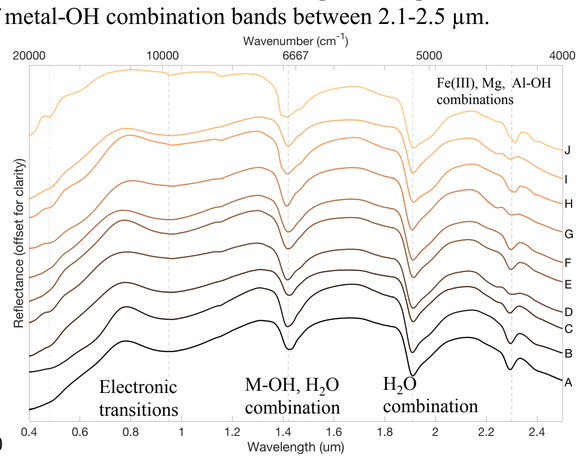


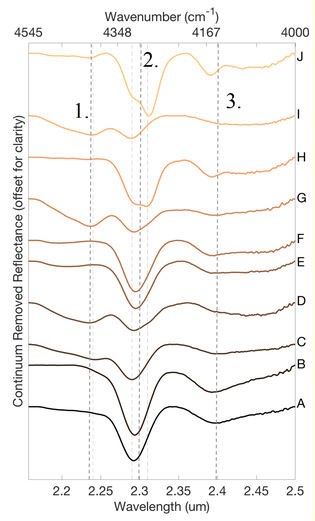


Metal-OH combination bands between 2.1-2.5 µm vary depending on the composition of the smectite octahedral layer. Circle size represents relative absorption depth, grey squares are derived from a compilation of di-octahedral smectite properties by Gates, 2005.

1.Al-M-OH Combination bands

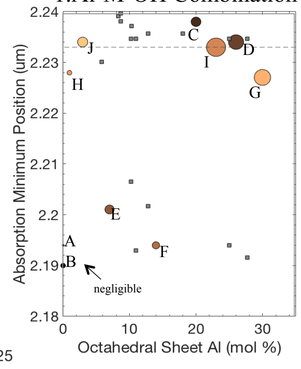


2.Fe(III)-OH, Mg-OH Combination bands

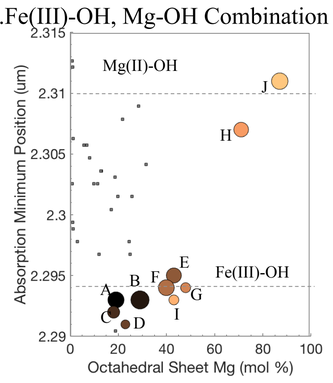


3.M-OH, Si-O Combination bands

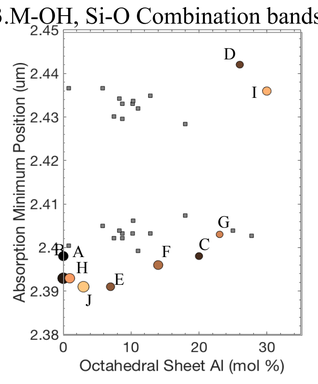


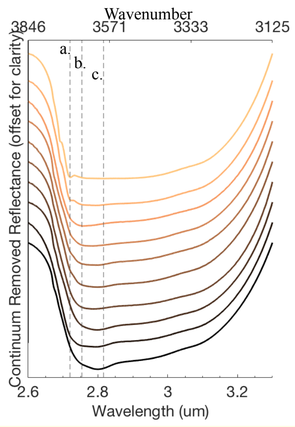


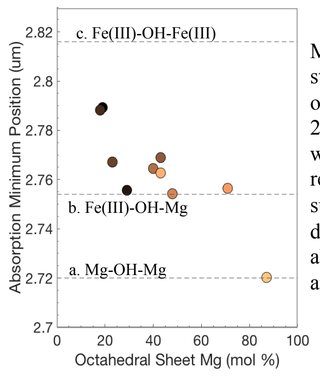


Metal-OH stretching mode occur in the 2.6-2.8 µm wavelength region, superimposed o deep $H_2O$ absorptions around 3 µm.

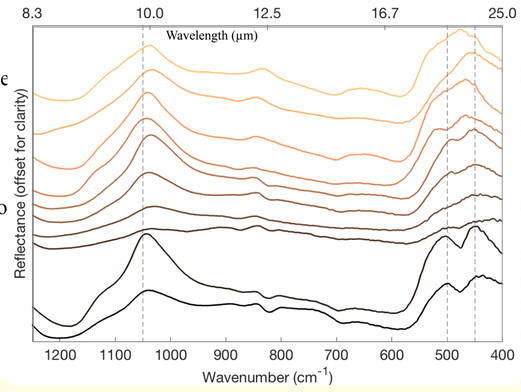


Tetrahedral layer Si-O bending and stretching modes occur around 1050 $cm^{-1}$ and 450-500 $cm^{-1}$, respectively. Features in the 650-800 $cm^{-1}$ region are Metal-OH bending modes.

## Ferrous Smectites

Octahedral layer composition of ferrous smectite samples.

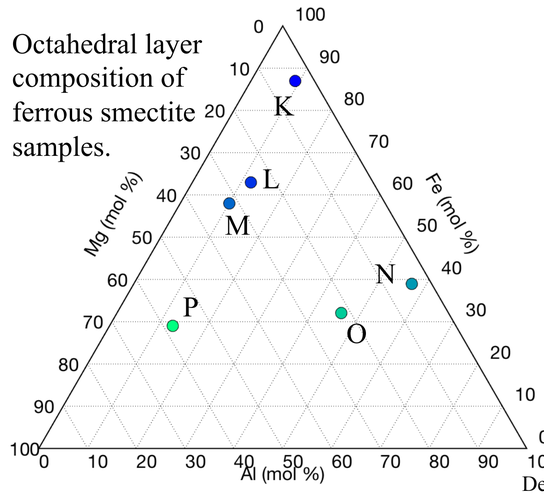


Deep 1.4 µm and 1.9µm absorptions indicate that ferrous samples are still significantly hydrated from synthesis.

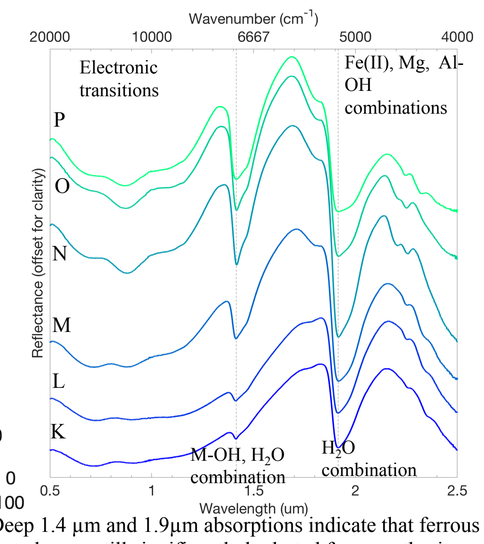


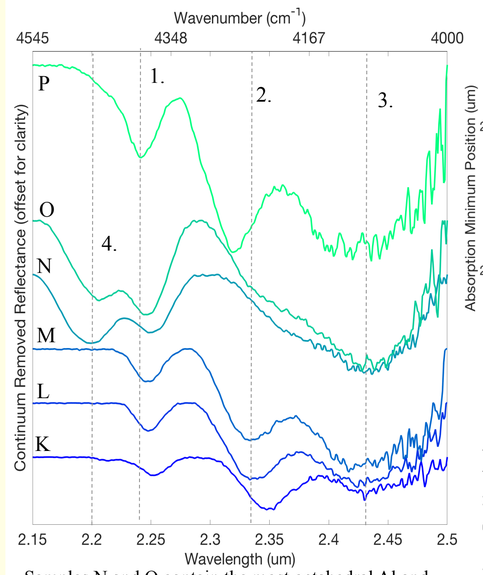


Samples N and O contain the most octahedral Al and XRD patterns (not shown) suggest that these samples are intermixed di- and tri- octahedral smectite phases. Such partitioning when synthesizing Al-Mg smectite series has been previously observed (Grauby et al 1993). More Fe(II) samples are being synthesized to better explore the compositional behavior.

1. Fe(II)-OH combinations

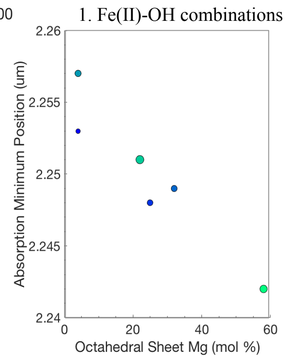


2.Mg(II)-OH combinations

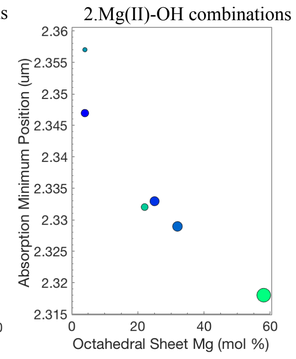


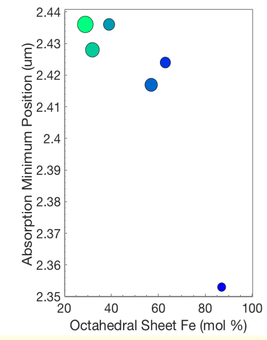


4.Al(III)-OH combination

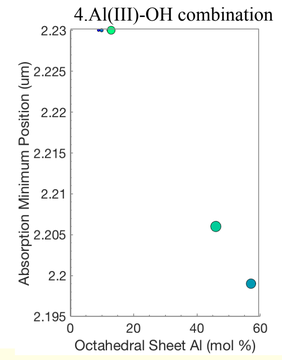


## Future Work

**Raman Spectroscopy: New Remote Sensing Technique on Mars**

The Mars2020 Rover carries two Raman spectrometers − SHERLOC and SuperCam − that will be the primary means of determining mineralogy on the mission.
We will characterize our sample set using analogous Raman techniques to provide spectral libraries of smectite clays to aid detection on Mars.

- Reflectance measurements in the Mid-IR and VSWIR will be used to calculate optical constants to improve quantitative mineral abundance modeling from planetary surface measurements.
- Smectite samples with intermediate oxidation states (Fe(II) and Fe(III)) are being synthesized to better understand understand mixed-valence clay spectral behavior.
- Samples will be measured to provide XRD patterns suitable for comparison to MSL CheMin observations.

## Practical Applications

### Understanding Clays in Gale Crater, Mars

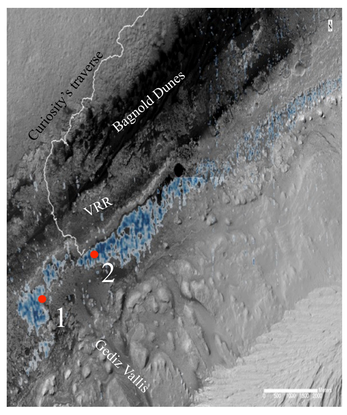


Clays on Mars are frequently identified as "Fe/Mg phyllosilicates"; this work could help better identify these phases.

The MSL rover approaches a region where smectite clays are detected from orbit (blue, left). The spectral character of these Fe/Mg clays are variable even within the identified unit. Regions near the hematite-bearing Vera Rubin Ridge (VRR) are consistent with Al-substituted nontronite. Areas more to the south have spectral features consistent with either more intermediate compositions or possible ferrous clays.

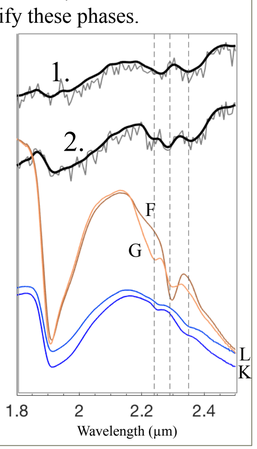


### Phyllosilicates throughout the solar system

IR analysis of Fe(II), Mg and Fe(III),Mg smectites is applicable to small bodies throughout the solar system.

Two new missions Hayabusa-2 and OSIRIS-REx will measure spectra of clay minerals in asteroids this summer

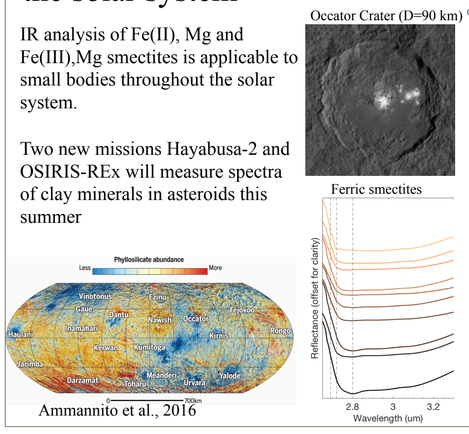


Ammannito et al., 2016

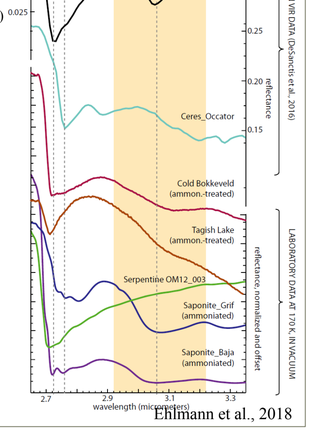


Ehlmann et al., 2018

This work is supported by a JPL topical RTD.

**National Aeronautics and Space Administration**
**Jet Propulsion Laboratory**
California Institute of Technology
Pasadena, California

www.nasa.gov



**Poster No. P-17**

National Aeronautics and Space Administration

# New tools for detecting carbonate-bearing surfaces on Mars: Possible detections of low-abundance carbonate in Noachian-aged crust

**Elena S. Amador (Caltech)**
**Bethany L. Ehlmann (3220; Caltech)**

## Why Search for carbonates on Mars?

- Martian carbonates provide clues to answering the question: **What were the earliest environmental and global conditions like on Mars?**
  - Transfer of $CO_2$ from atmosphere to crust via carbonates may be an important process in its loss (Edwards and Ehlmann 2015 Geology; Hu+ 2015 Nat Comm).
  - Surface exposures of carbonate account for only a small percentage of secondary phases presently detected on the surface of Mars (Niles+ 2013 Space Sci Rev; Ehlmann and Edwards 2015 Annu. Earth Rev.).
  - This paucity has implications for the evolution of the martian climate, as carbonate should form readily under a $CO_2$-rich atmosphere and surface water (Kahn 1985 Icarus; Pollock+ 1987 Icarus).
- **Given the "warm/wet" vs. "cold/dry" early Mars paradigm, knowing the global distribution of exposed carbonates may support one model over another.**
  - This has important implications for **where** sustained **habitable environments** may have existed on early Mars.

## Factor Analysis and Target Transformation (FA/TT)

### Study and Method Objectives

- This work aims to search for carbonate spectral signatures using statistical tools that can tease out signatures that may otherwise be missed.
- Factor analysis and target transformation (FA/TT) is a principal-components based method that can identify spectral endmembers that may not exist on the surface in pure unmixed form (Malinowksi+ 1991 Wiley).

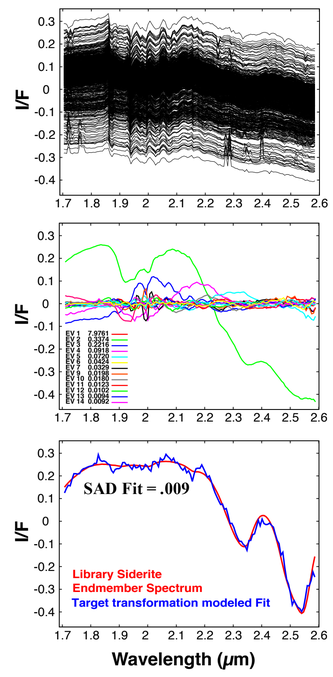


**Raw CRISM I/F Spectra**

**Factor Analysis**

We use factor analysis to reduce a complex set of CRISM spectra to a few spectral shapes that contain all the spectral variations present within the images.

Typically 15-20 eigenvectors

**Target Transformation**

We use target transformation, a leasts squares fitting routine, to reconstruct the tested endmember (e.g., siderite) using the calcuated eigenvectors.

A strong fit between the reconstructed data and the test endmember indicates that the endmember is likely a constituent of the image.

**Spectral Angle Distance (SAD)**
A measure of "goodness of fit"
**Lower SAD value == higher spectral similarity**

We used the SAD parameter in two ways:
1) Quantify spectral fit between modeled spectra and endmember spectra.
2) Test the spatial distribution of the modeled target transformation spectrum to individual image pixels.

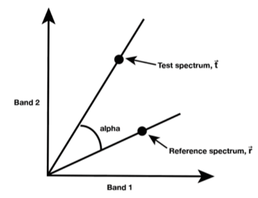


$$SAD = cos^{-1}\left(\frac{\vec{t}\cdot\vec{r}}{\|\vec{t}\|\cdot\|\vec{r}\|}\right)$$

Where:
t = Moded target transformation fit spectrum (band 1)
r = Library endmember spectrum (band 2)

## Examples of technique validation

Extensive work (Thomas and Bandfield 2017 Icarus; Amador+ 2018 Icarus) has shown that FA/TT can robustly recreate and identify carbonate in Nili Fossae – a region that has been well documented as containing carbonate-bearing rocks.

Additionally, our current work has provided several new examples of method validation:
- Confirming carbonate non-detections in Cross Crater where alunite (sulfate) has been detected and non-detections in Gale Crater corroborating MSL results
- Independently detecting Mg-carbonate where it has been identified in-situ by rovers (Columbia Hills)
- Confirming the null case in dusty images where there should be no spectral fits
- Working with terrestrial hand samples and laboratory acquired spectral images (**below**)

### Serpentinite hand-sample from the Oman Ophiolite imaged by UCIS at JPL

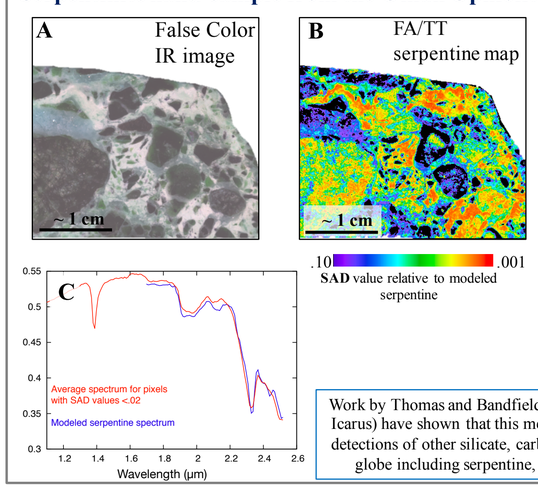


**(A-B)** show a serpentinite hand sample from the Oman Ophiolite. FA/TT methods can be tested against a sample like this with known mineralogical composition. **(C)** shows a strong modeled fit (blue spectrum) to serpentine and fits well to the average reflectance spectra (red spectrum) for pixels in the image (red pixels in **B**) correctly IDed as serpentine-bearing.

Work by Thomas and Bandfield (2017, Icarus) and Amador+ (2018, Icarus) have shown that this method can independently corroborate detections of other silicate, carbonate, and sulfate phases across the globe including serpentine, kaolinite, kieserite, and gypsum.

**Global map of all CRISM images from 60 to -60 °N analyzed with the FA/TT method.** Colorized **circles** (magnesite) and **squares** (siderite) indicate the CRISM images with target transformation SAD values <~0.02, which indicate a high spectral similarity to the tested carbonates phase. Colorized **points** indicate images with poor spectral fits. Overlain on MOLA DEM. FA/TT indicate similar global carbonate patterns to those identified with traditional CRISM analysis techniques (Wray+ 2016 JGR-Planets).

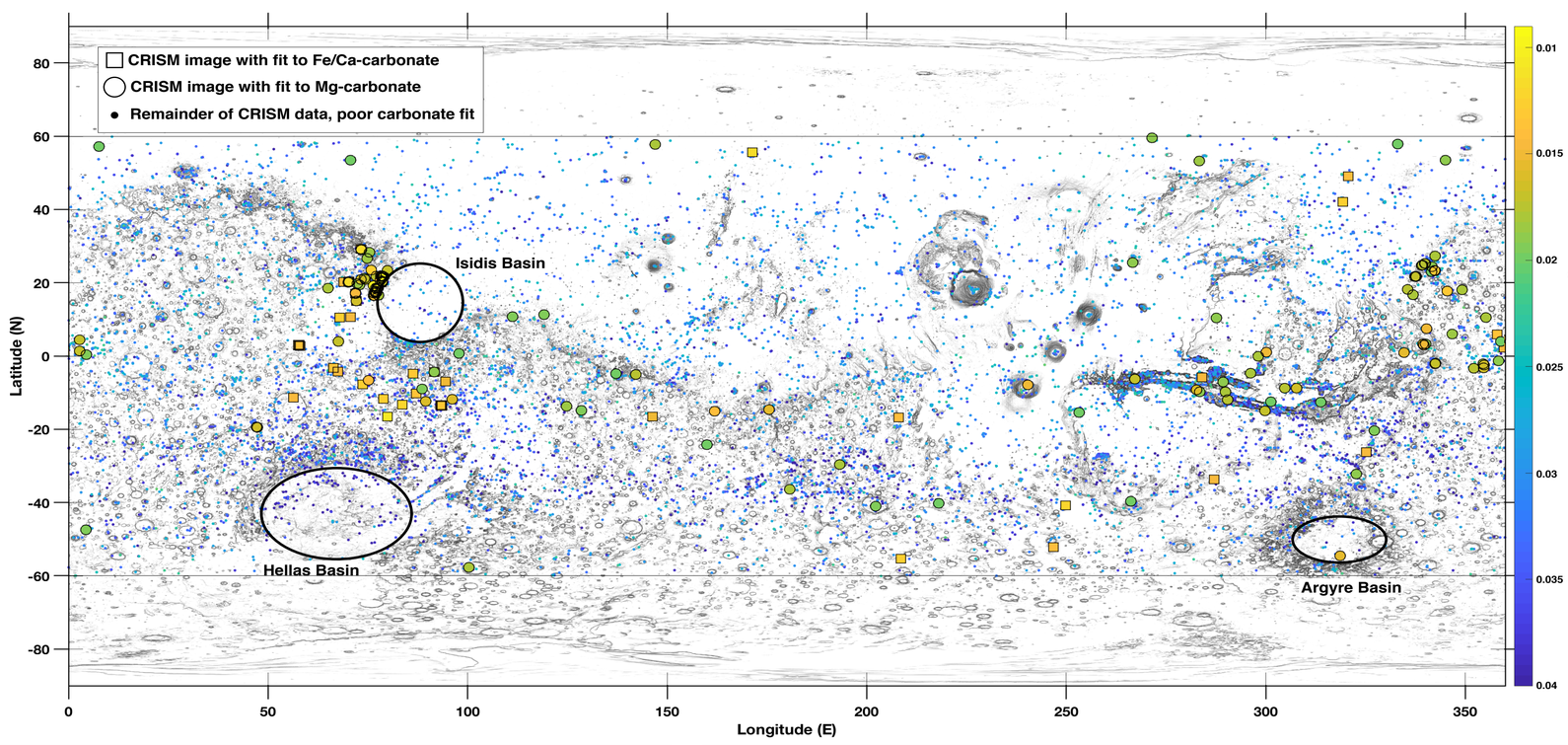


## Example region: Nili Fossae

Across the planet, CRISM images with the strongest spectral fits to Mg-carbonate endmember are found in eastern Nili Fossae (**right**) – as described by numerous previous studies.

New, are strong spectral fits to a Fe/Ca-carbonate endmember in western Nili Fossae near Toro and Negril Craters (**A**). These fits are also in association with a Mg-carbonate component and hydrated silica (previously described) – pointing at a more evolved aqueous alteration history.

This technique can also be used to better understand spectral mixtures. More rigorous FA/TT analysis of the carbonate-bearing spectra in Jezero Crater (*a potential landing site for the Mars 2020 rover*) points to a Mg-carbonate + serpentine mixture as the most dominant spectral component (**B**) - hinting at preserved mineralogical evidence for a once habitable environment (serpentinization).

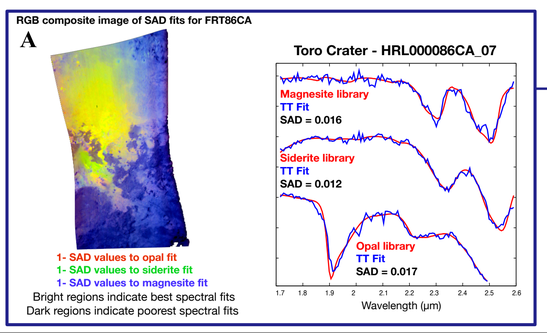


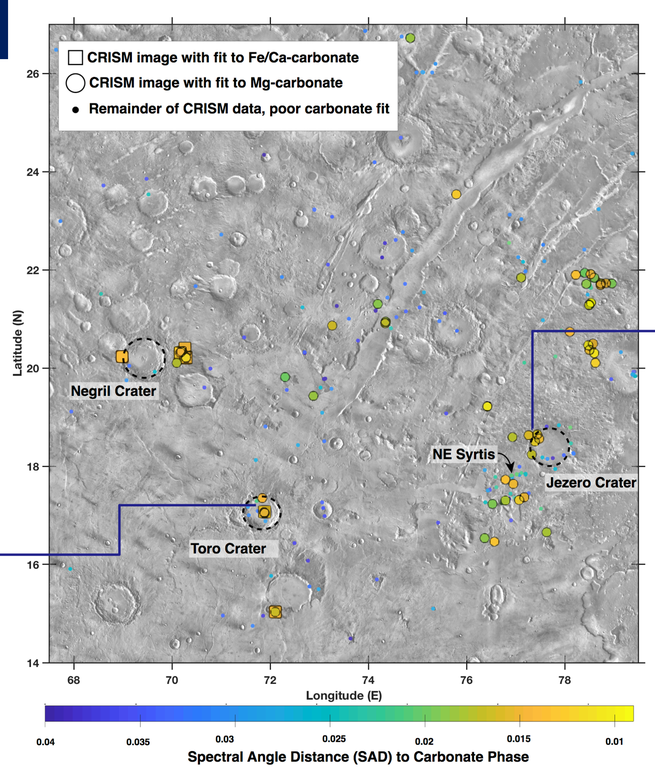


**B** HRL 40FF in Jezero Crater

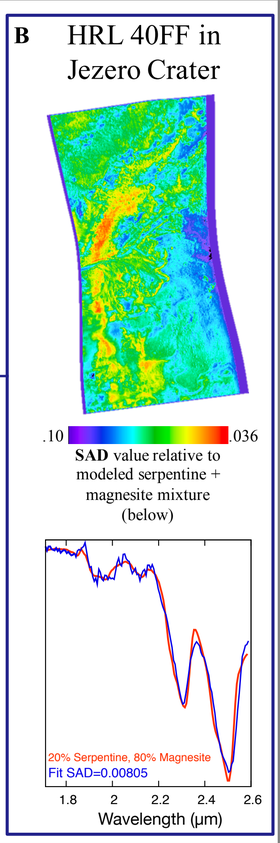


## Preliminary Implications and Conclusions

- The FA/TT method has allowed for the ID of, and distinction between, carbonate phases across Mars.
- Phases identified in W. Nili Fossae (shown here) and scattered across the globe, show two separate spectral groups (**right**) which may indicate multiple episodes of carbonate formation in various geochemical redox conditions that have subsequently been exhumed.
- Ultimately, these strong fits to carbonate represent a spectral component occurring in these images that is similar to carbonate. Given that they are often not observable in direct I/F observations, they likely represent a surface component that exists at low spectral variance, probably due to low abundances, across the image. *They may represent a yet undetected reservoir of low abundance carbonate found in Noachian crusts.*

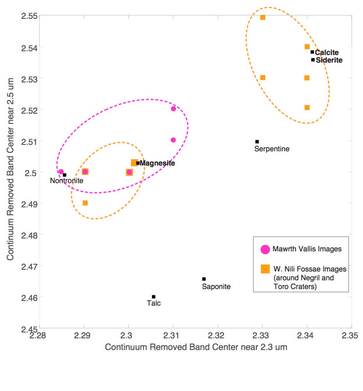


- **Even with the discovery of dozens of new carbonate exposures (see global map above), carbonate is still rarely observed on the surface of Mars today, relative to other secondary phases. This may support a model where Mars lost its atmosphere very early and that warm/wet periods were cyclical and not sustained – subsurface habitable environments may have thus been longer lasting throughout Mars' history.**

**Acknowledgments**: Special thanks to David Thompson (JPL) and Murat Dundar (Indiana University) for helpful discussion regarding this work.

**National Aeronautics and Space Administration**
**Jet Propulsion Laboratory**
California Institute of Technology
Pasadena, California

www.nasa.gov

**Poster No. P-18**